This paper is a non-peer reviewed EarthArXiv preprint and is currently under review at a scientific journal.

Unexpected canopy gain in Earth's mangrove forests linked to natural

expansion and regrowth 2 3

4 5

Zhen Zhang^{1*}, Nicholas J. Murray², Xiao-Peng Song³, Pete Bunting⁴, Thomas A. Worthington⁵, Lola Fatoyinbo^{6,7}, Dehua Mao⁸, Mingming Jia⁸, Virni Budi Arifanti⁹, Toh Aung¹⁰, San San Htay¹¹, Daniel A. Friess^{1*}

6 7

8

9

10

11

14

16

17 18

20

21

1

- 1. Department of Earth and Environmental Sciences, Tulane University, New Orleans, LA, USA.
- 2. College of Science and Engineering, James Cook University, Townsville, Australia.
- 3. Department of Geographical Sciences, University of Maryland, College Park, MD, USA.
- 4. Department of Geography and Earth Sciences, Aberystwyth University, Aberystwyth, Wales, UK.
- 5. Department of Plant Sciences, University of Cambridge, Cambridge, UK.
- 12 6. Space Enabled Research Group, Department of Media Arts and Sciences, Massachusetts Institute of Technology,
- 13 Cambridge, MA, USA.
 - 7. Biospheric Sciences Laboratory, National Aeronautics and Space Administration (NASA) Goddard Space Flight
- 15 Center, Greenbelt, MD, USA.
 - 8. Key Laboratory of Wetland Ecology and Environment, Northeast Institute of Geography and Agroecology, Chinese
 - Academy of Sciences, Changchun, China.
 - 9. Research Center for Ecology, National Research and Innovation Agency of the Republic of Indonesia, Cibinong,
- 19 Indonesia.
 - 10. Natural Resources Governance and Environment, Yangon, Myanmar.
 - 11. Climate Change and Blue Carbon Program, Yangon, Myanmar.

22 23

*Corresponding authors: zzhang58@tulane.edu; dfriess@tulane.edu

24

25

26

27 28

29

30

31 32

33

34

35 36

37

Abstract

Mangroves have disappeared rapidly due to deforestation and sea-level rise but can also recover through natural regrowth and restoration. However, their long-term trajectory in area and canopy cover remains highly uncertain. By developing a global mangrove canopy density dataset, we show that mangrove loss (conversion to other land uses) and degradation (reduction in canopy density) have been reduced and have been largely offset by regeneration and natural seaward expansion over four decades. As a result, global mangrove extent has reversed from net loss to net gain and shown a decline of only around -1% from the 1980s to 2023, although most newly established mangroves still provide limited ecosystem services because they are not yet mature enough to compensate for the loss of older forests. Meanwhile, persistent mangrove forests keep accumulating canopy density, suggesting natural growth and potential underestimation of blue carbon gains in current area-based assessments. Our results reveal the underestimated resilience of a highly threatened ecosystem and suggest halting deforestation as a priority to meet global restoration targets through natural regrowth.

Conserving and restoring coastal wetlands represents a promising nature-based pathway to protect biodiversity (I), enhance coastal resilience (2), and mitigate climate change (3). Recognized for their ecological importance, coastal wetlands have become central to major international restoration initiatives, such as the Bonn Challenge and the UN Decade on Ecosystem Restoration. Mangrove forests, in particular, have emerged as a focal point in coastal restoration efforts (4), given they support a wide range of ecosystem services including coastal protection, fishery support, climate regulation, and cultural values (5). Historically, mangroves have been subjected to extensive deforestation because of development such as aquaculture, oil palm plantations, and rice paddy agriculture (6-8). Additionally, natural disturbances, including tropical cyclones and shoreline erosion, pose serious threats to mangrove ecosystems (9, 10). As a result, global assessments have consistently concluded that mangroves remain in a state of long-term decline (11, 12).

To halt and reverse this trend, numerous countries have launched ambitious mangrove restoration initiatives, such as Indonesia's National Mangrove Conservation Programme (13) and the United Arab Emirates' pledge to plant 100 million mangroves by 2030 (14). Some countries have already shown signs of success, such as the rebound of mangrove areas in China following the implementation of strong protection policies (15). While such interventions may slow deforestation rates (6), they have not yet fully reversed the trajectory of global mangrove loss. Besides assisted restoration, mangroves possess a strong capacity for natural expansion. Riverine sediment deposition creates newly accreted mudflats that offer suitable habitats for mangrove colonization (11, 16), facilitating seaward expansion into previously unvegetated areas (17). Mangroves also have the potential to regenerate within abandoned aquaculture ponds, provided that environmental conditions remain favorable (8). However, the extent to which these processes of expansion and regeneration have offset historical mangrove losses remains poorly understood.

Even in the absence of complete deforestation, mangrove canopy cover can undergo damage due to both natural disturbances [e.g., cyclones (18) and climatic oscillations (19)] and anthropogenic impacts (e.g., selective logging), a process referred to as degradation (20, 21). Such degradation has a range of ecological consequences, including carbon release, reduced coastal protection, and loss of biodiversity (22). Nevertheless, mangroves are known for their resilience to disturbance. For instance, they can recover to pre-cyclone level of leaf area within just one year (23). Yet, little is known about the global rates and spatial extent of mangrove degradation and growth.

Here we quantified global mangrove canopy dynamics by developing a high--resolution (30 m) annual product of mangrove extent and Fractional Canopy Cover (FCC) from 1984 to 2023. Annual mangrove extents were categorized into four canopy conditions, including closed mangrove forests (FCC > 80%), open mangrove forests (50%-80%), mangrove woodland (20%-50%), and sparse mangroves (< 20%) (24) (fig. S1). Four types of mangrove dynamics were then distinguished: loss, defined as complete conversion of mangroves to other land covers for at least 3 years, whether driven by natural or anthropogenic factors (deforestation); gain, new mangroves gained from lost mangrove forests (regeneration) or from areas that were not previously mangrove within our time series (expansion); degradation, defined as a downward transition between mangrove canopy types accompanied by a minimum FCC decline of 20% within persistent mangroves (25), or as a short-term loss of mangroves (< 3 years) (26); and growth, defined as a substantial increase in FCC of persistent mangrove areas (27, 28), namely the opposite of degradation. Through this approach, we first analyzed long-term trajectories of global and regional mangrove extent since the 1980s, followed by trends in loss and degradation rates, and finally assessed mangrove growth, with particular attention to those persistent mangrove forests without land-cover changes.

Results

A shift from net loss to net gain

Four decades of satellite monitoring reveal a reversal in the global trajectory of mangrove extent. Between the 1980s and 2010, global mangrove extent declined from 154,810 km² [95% confidence interval (CI): 140,661 to 158,069 km²] to 151,928 km² (139,539 to 154,633 km², 95% CI), representing a net loss of 2,882 km² (1.86%, 95% CI: -4,939 to 1,025 km²). However, this trend reversed in the subsequent decade. By 2023, global mangrove area had rebounded to 153,961 km² (145,085 to 158,206 km², 95% CI), reflecting a net gain of 2,033 km² (1.34%, 95% CI: 1,131 to 3,158 km²) since 2010 and resulting in a marginal net loss of just 848.8 km² (95% CI: -2,927 to 1,360 km²) over the entire 1980s-2023 period (table S1). This small net loss underscores the substantial compensatory effect of mangrove gains. Between the 1980s and 2010, 12,657 km² or 8.2% (10,283 to 14,317 km², 95% CI) of mangroves were lost, yet 9,775 km² (7,467 to 11,566 km², 95% CI) of new mangrove forests were established, mitigating 77% of gross losses. From 2010 to 2023, mangrove gain accelerated from an average of 0.28% per year to 0.42% per year, contributing 8,307 km² (6,660 to 9,492 km², 95% CI) of new growth that outpaced 6,275 km² (4,539 to 7,696 km², 95% CI) of loss (table S1).

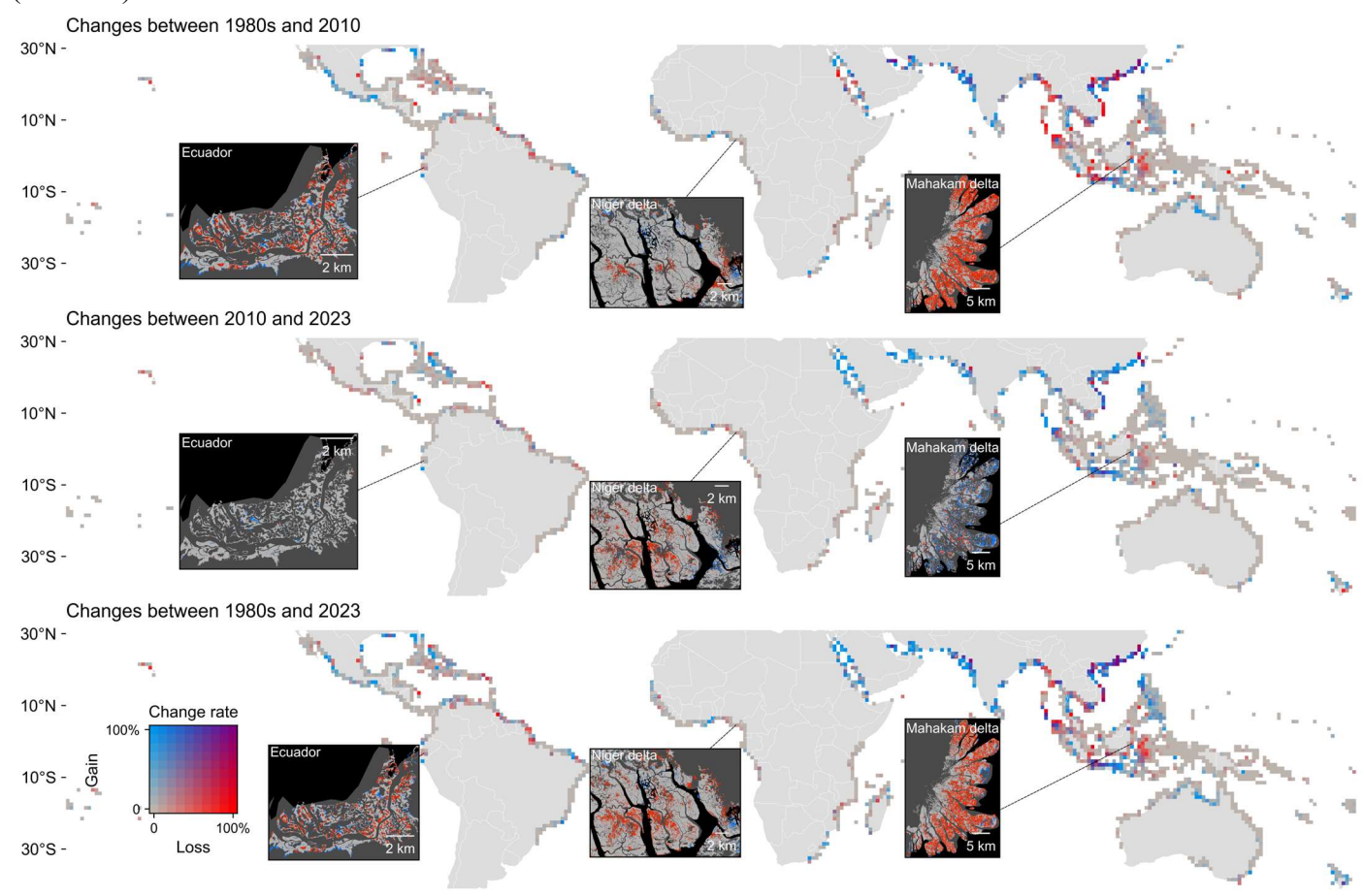


Fig. 1. Global pattern of mangrove loss and gain during 1980s-2023. The color scale, shown on the bottom left, indicates the rate of change in terms of both loss (red) and gain (blue), with 0% change represented by grey. The rate is calculated as (Δarea/original area) × 100%. Inset regional maps provide detailed examples of change patterns for Ecuador, the Niger Delta of Nigeria, and the Mahakam Delta of Indonesia, where blue patches indicate mangrove gain, red patches signify loss, and grey patches indicate persistent mangrove areas. An online interactive map for mangrove extents and their change area is available through the following link: https://zhenzhang.users.earthengine.app/view/globalmangrovedynamic.

Separating global signals by biogeographic region (fig. S2) reveals that net mangrove loss from the 1980s to 2010 was overwhelmingly concentrated in Southeast Asia (table S1), which accounted for 59.3% of global mangrove losses, followed by Americas (22.5%). Key hotspots included Kalimantan, Sulawesi,

Sumatra, Myanmar, the Caribbean, and parts of Brazil (Fig. 1). Notably, the rate of net loss in Southeast Asia peaked between 1990 and 2005 but has since slowed, with the region transitioning to net gain after 2010 (Fig. 2A). This shift was dominated by Indonesia (fig. S3 and fig. S4), where rapid mangrove loss between 1995 and 2005 was followed by a notable stabilization, and gain in Myanmar in which mangrove cover transitioned from consistent decline to net gain after 2010 (fig. S3 and fig. S4), particularly in the Irrawaddy Delta, Gulf of Martaban, and Rakhine State, including the Naf River region along the Myanmar-Bangladesh border (fig. S5). Despite a 10% increase in mangrove area since 2010, Myanmar experienced a net loss of 28.6% between the 1980s and 2010, making it still the most severely deforested country among major mangrove-holding nations (Fig. 2E). In contrast, West and Central Africa have shown the opposite trend. After decades of expansion, particularly in Senegal, Gambia, and Guinea-Bissau, the region shifted to net loss around 2014, driven by accelerating losses in Nigeria since 2002 (fig. S3).

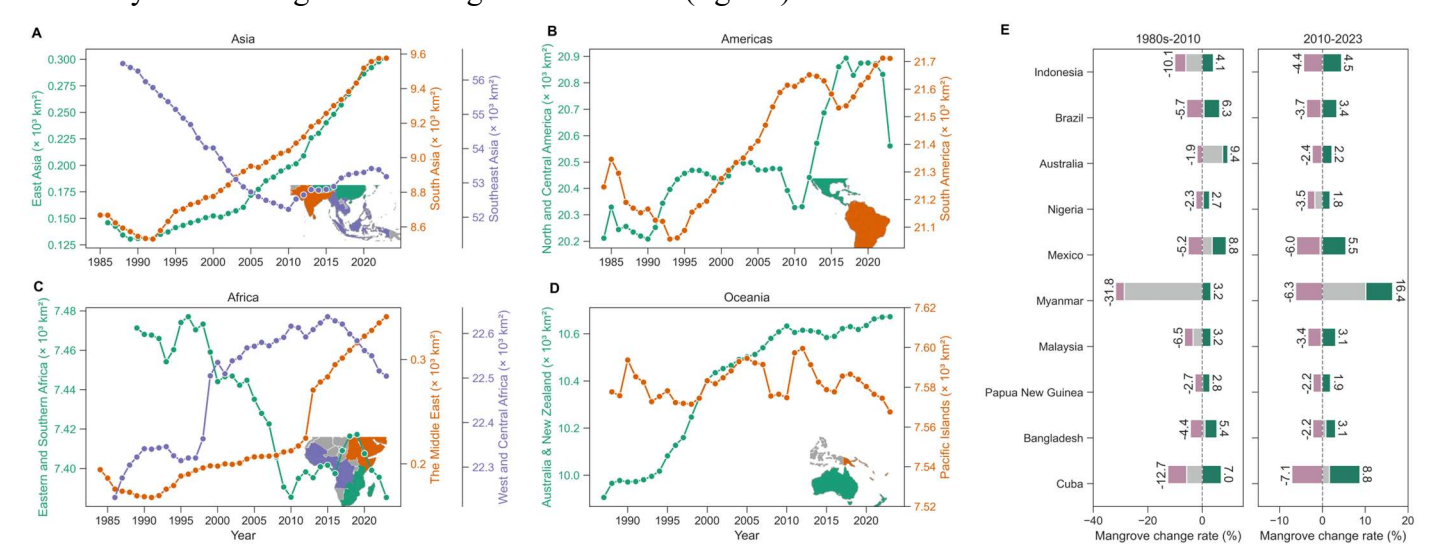


Fig. 2. Regional mangrove area dynamics and country-level change rates. A-D, Time series of mangrove areas (km²) from the late 1980s to 2023 for (**A**) Asia, (**B**) Americas, (**C**) Africa, and (**D**) Oceania. Within each continental plot, individual lines represent distinct biogeographical regions, with corresponding geographical extents shown in the inset maps in matching colors. For enhanced visualization, the Middle East is grouped with Africa. **E**, Mangrove change rates for the top 10 mangrove-rich nations in the 1980s, ordered by their mangrove extent. Teal bars indicate gain rates, pink bars show loss rates, and grey bars represent the net change rate.

Outside of Southeast Asia and Africa, all remaining regions exhibited long-term net gains in mangrove areas (Fig. 2A-D), particularly pronounced in northern Australia, western Mexico, the Gulf of Mexico, the Middle East, and South Asia (Fig. 1). Specifically, in Australia and New Zealand, mangrove gains were most rapid between 1987 and 2010 (Fig. 2D); South Asia, East Asia, and the Middle East each demonstrated near-linear increases in mangrove extent since the 1990s (Fig. 2A and C).

Our analysis also differentiated between mangrove expansion (i.e., the establishment of mangroves in areas lacking mangrove cover in 1980s) and regeneration (i.e., regrowth within mangrove areas that were formerly deforested). Of the 7,476 km² of global gains from 2010 to 2023, expansion accounted for 5,364 km² (64.6%), with regeneration comprising the remaining 35.4%, suggesting an expansion-dominated mangrove gain (Fig. 3). Expansion usually occurred in deltaic and riverine areas (Fig. 3C-F), consistent with natural colonization processes. A striking hotspot of mangrove expansion is the northeastern coastline of South America, where mudbanks formed by Amazon River sediment provide new habitats for rapid mangrove colonization (29). This reflects the ecological adaptability of mangroves to colonize bare mudflats when environmental conditions are within their physiological tolerance (30). Observed mangrove gains also align with reported net mangrove gains in global deltas due to increased sediment input from upstream deforestation

and mining (16, 31), reflecting that the rate of mangrove gain in minerogenic settings highly depends on terrigenous sediment supply.

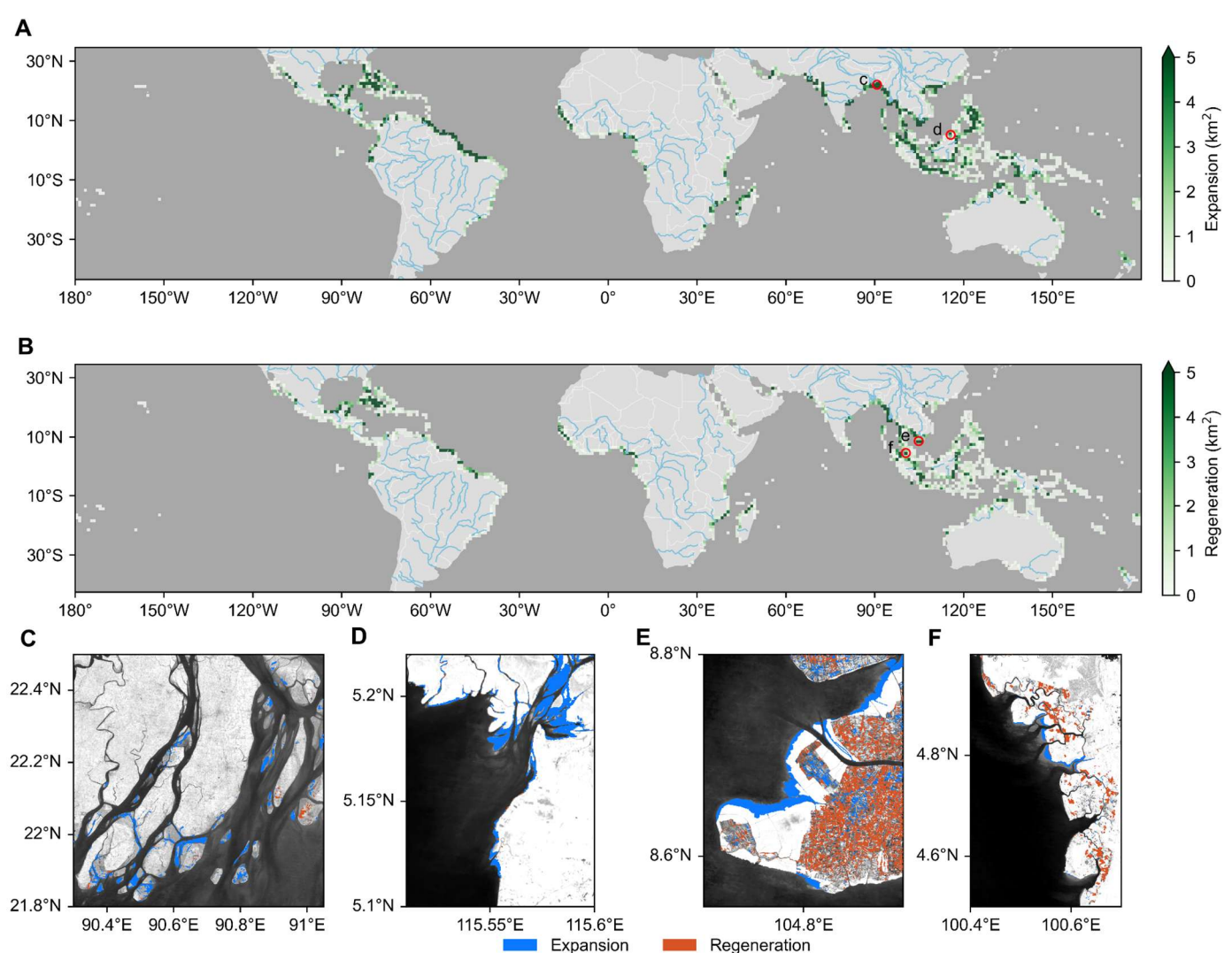


Fig. 3. Global pattern of mangrove expansion and regeneration (2010-2023). A, Global distribution of mangrove expansion. The color scale indicates the expansion area in km² per grid cell. B, Global distribution of mangrove regeneration, with the same color scale as in A. The blue lines in panels A and B represent major rivers. The red dots in panels A and B indicate the locations of the regional examples shown in panels C-F. The background imagery for panels C-F is a Landsat 8 near-infrared composite from 2023.

Mangrove degradation and loss are slowing down

On average, annual degradation rates exceeded loss rates across 64.9% of global mangrove area, being particularly evident in Africa, the Caribbean, and the Pacific Islands (Fig. 4A). Southeast Asia exhibited high rates of both degradation and loss, especially in mainland regions. In certain years, degradation was several-folder higher than loss, such as in South Asia (2008), Eastern and Southern Africa (2000), North and Central America (2017), and Australia and New Zealand (2011) (Fig. 4B). These abrupt degradation events coincided closely with the passage of tropical cyclones (fig. S6), including Cyclone Yasi in Australia (2011), Hurricane Irma in Cuba and Florida (2017), Cyclone Rashmi in the Sundarbans (2008), and Cyclone Leon-Eline in Mozambique (2000), confirming tropical cyclone as a dominant driver of mangrove degradation globally. Human activities have also played an important role in mangrove degradation. For example, crude oil pollution has caused extensive and long-term damage to mangrove ecosystems in the Niger Delta (32).

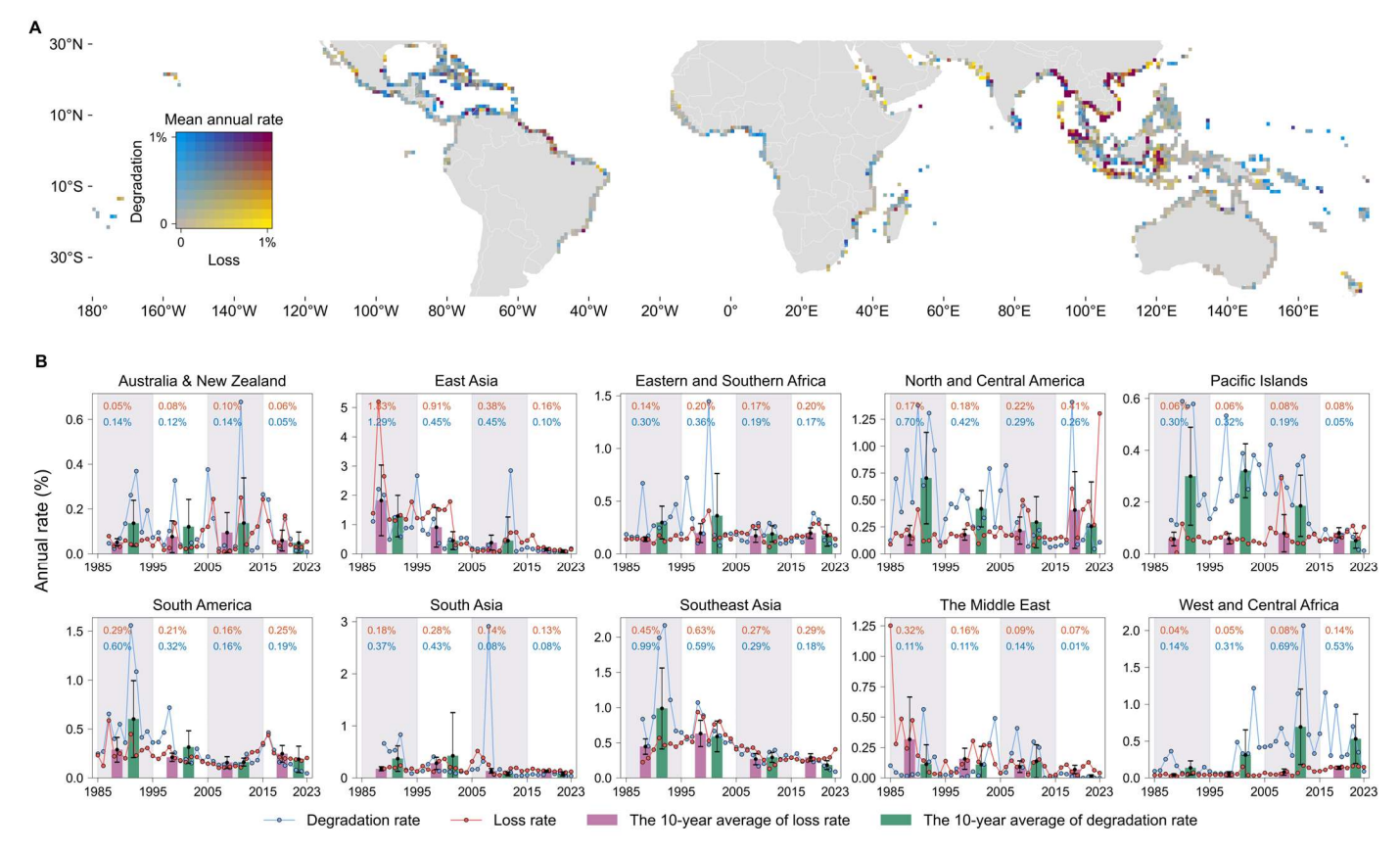


Fig. 4. Global and regional rates of mangrove disturbance consisting of loss and degradation. A, Global pattern of long-term average annual disturbance rates. The color key indicates the mean annual rate, with increasing degradation towards blue and increasing loss towards yellow, with red representing high rates of both and grey representing low rates for both. **B**, Temporal profiles of annual rates for ten biogeographical regions. Individual points and thin lines show the annual rates of loss (yellow) and degradation (blue). Temporal peaks in disturbance rates align closely with tropical cyclone events, such as Cyclone Rashmi in 2008 in South Asia (fig. S6). The bars represent the 10-year average rate of loss (pink) and degradation (green), with error bars indicating the corresponding 10-year standard deviation. Numbers within each regional panel correspond to the 10-year average rate for loss (red) and degradation (blue).

 Mangrove disturbance (i.e., degradation and loss) rates have declined over the past four decades, mostly from degradation, which fell from approximately 0.64% yr⁻¹ in the 1980s to 0.24% yr⁻¹ by the recent decade (fig. S7). The average loss rate of mangroves during the recent decade was also around 0.24% yr⁻¹, comparable to 1985-1995 but lower than 1995-2005 (0.33% yr⁻¹), suggesting a decline in mangrove loss rate since 2000. Southeast Asia exhibited substantial decrease in annual rates of both mangrove degradation and loss (Fig. 4B). We observed an initial rise in loss rate between 1988 and 1998, followed by a decline to 2011, after which rates stabilized at around 0.29% yr⁻¹. These patterns are consistent with previous findings (6, 33, 34) and reflect the cumulative impact of conservation efforts (4), reduced tropical cyclone frequency in some regions (35), and increased agroforestry practices (36). However, these declines in disturbance were partly offset by rising rates in West and Central Africa, which has emerged as the current hotspot of mangrove degradation, reaching ~0.53% yr⁻¹ during 2015-2023, primarily concentrated in the Niger Delta (fig. S8).

Despite an overall reduction, mangrove disturbance still persists in recent years (2018-2023) (fig. S9). Some of these events were associated with climatic drivers, such as mangrove dieback in Texas following a severe freeze in 2020, damage from Hurricane Ian in Cuba and Florida (2022), and canopy loss in Mexico's Marismas Nacionales-San Blas mangroves following Hurricane Roslyn (2022) (fig. S10). Shoreline erosion still contributes to mangrove loss, such as along the Amazon-Guianas Atlantic coastline (fig. S10C). Anthropogenic deforestation, however, remains widespread, even within formally protected areas. A striking

example is the Rufiji Delta in Tanzania, which is a Ramsar wetland conservation site but is experiencing excessive mangrove deforestation due to cropland expansion and timber production (37) (fig. S10E).

Increased canopy density of mangrove forests

Although abrupt mangrove degradation events have occurred in specific years, a broader decadal perspective reveals a net gain in canopy cover, as evidenced by an increase in the extent of closed-canopy mangrove forests (FCC > 80%). Globally, closed mangrove forests increased from 77,643km² (50.2% of total mangrove area) in the 1980s to 88,772km² (57.7% of total) by 2023, even though total mangrove area has slightly decreased. Increases in closed mangrove forests from 1980s to 2023 were considerably high in South America [31.2% (3,548 km²) of total increases], mostly taking place along the Amazon Macrotidal Mangrove Coast (Fig. 5A, B). Closed mangrove forests in the Middle East, western South Asia, and East Asia experienced large increases in terms of proportion (fig. S11), probably due to range expansion (38) and restoration efforts (39). Eastern and Central Africa is the only biogeographic region with decreased closed mangrove forests, concentrated mostly in Madagascar (Fig. 5A).

Although closed mangrove forests show a net global gain, they are also more vulnerable to loss compared to sparser mangroves. Between the 1980s and 2023, closed mangroves alone accounted for nearly half (48.6% or 6,866 km²) of gross mangrove loss, two-thirds of which (66.7% or 4,581 km²) occurred in Southeast Asia. Since mangrove losses in Southeast Asia are largely driven by anthropogenic factors (6), this suggests that commodity-driven deforestation disproportionately targets mature, high-density mangroves. However, this loss has been partly offset by concurrent growth in new mangroves, 42.8% (5,679 km²) of which has grown into closed-canopy condition by 2023 globally. The formation of closed mangrove forests can occur rapidly. For example, 33.5% (2,783 km²) of young mangroves established since 2010 had transitioned to closed-canopy condition by 2023, with expansion slightly more likely to achieve closure (34.8 %) than regeneration (31.2 %).

The largest contributor to the net increase in closed mangrove forests is from persistent mangroves, those without replacement from the 1980s to 2023. In the 1980s, 50.3% of persistent mangroves had closed canopies; by 2023, this proportion had risen to 59.2%, largely due to transitions from open-canopy mangroves (Fig. 5D). Even in Southeast Asia, where closed mangrove forests have been substantially lost, increased canopy cover in those persistent mangroves compensated for the loss and made the area of closed mangrove forests in Southeast Asia stable. These results demonstrate that, in the absence of loss, mangrove forests have a strong capacity to increase canopy density, which is consistent with observed increased mangrove greenness (40) and can contribute to increased mangrove productivity (41). As of 2023, 42.3% of global mangrove forests remain in an open or woodland state, with some representing a substantial potential reservoir for future natural closed-canopy development under effective protection.

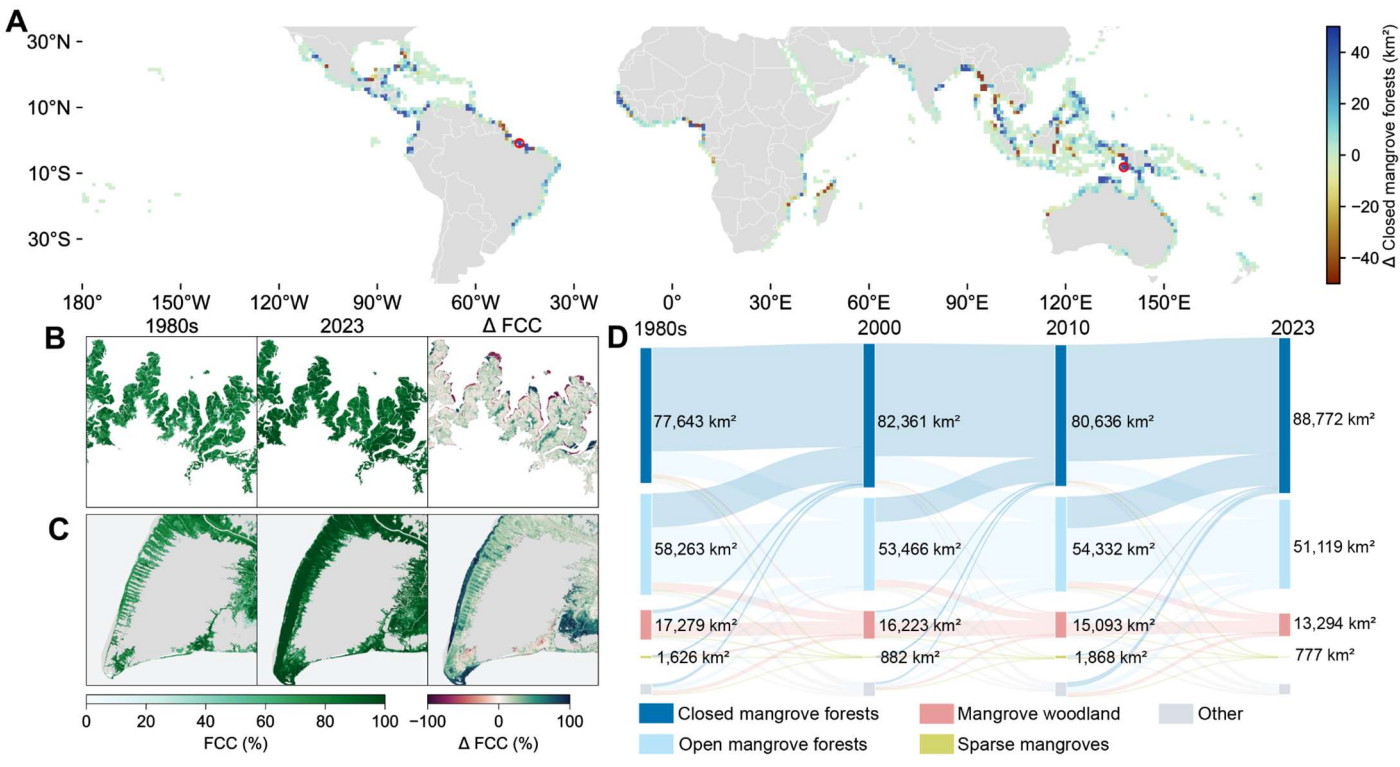


Fig. 5. Dynamics of mangrove canopy cover. A, Global pattern of area change (km²) of closed mangrove forests from the 1980s to 2023. The color map indicates the magnitude of change, with blue representing increases and red representing decreases in area. The two red circles highlight the locations of the regional examples detailed in panels **B** and **C** (Amazon Macrotidal Mangrove Coast and southwestern Papua, respectively). **B** and **C**, Regional examples illustrating mangrove change. For each region, the left and middle sub-panels display FCC images from the 1980s and 2023, respectively, where darker green indicates higher canopy cover. The right sub-panels show the change in FCC (Δ FCC = 2023 FCC - 1980s FCC), with greener areas indicating increased FCC (i.e., mangrove growth). **D**, Sankey diagram illustrating the flow and area (km²) of different mangrove canopy types across four time points: 1980s, 2000, 2010, and 2023, which highlights the overall increase in closed mangrove forest area, primarily transferred from open mangrove forests.

Discussion

Our results reveal widespread mangrove expansion and regeneration, which runs counter to earlier global assessments, including the Global Tidal Wetland Change (11) and Global Mangrove Watch (GMW) (12), which reported persistent declines across all biogeographic regions (fig. S12). However, at a regional and national level, our findings are consistent with emerging studies documenting mangrove gains in Australia (24), East Asia (15, 39), Senegal (42), Brazil (43), and the Middle East (44, 45), and show a substantial underestimation of mangrove gains in previous assessments (fig. S13).

We found a recovery in mangrove areas of Southeast Asia, the hotspot of mangrove deforestation. This finding aligns with local evidence, including seaward expansion in several major deltas of Southeast Asia (17), reduced mangrove disturbances in Myanmar after 2010 (46), and notable post-2010 mangrove expansion in parts of Indonesia (47) and Myanmar (7, 48, 49). Our detected reversal in Myanmar is also robust across two independent mapping approaches (fig. S5B). In Indonesia, mangrove dynamics can be explained by heightened awareness and restoration following the 2004 tsunami (13), and improved legal protection for mangroves since the early 2000s (50), particularly cross-sectoral coordination mechanisms for mangrove management and legal mechanisms for community management (51). Private sector and community initiatives have also led to increased mangrove planting efforts across Indonesia. Mangrove dynamics in Myanmar can be explained partly by increased awareness following the devastating impact of Cyclone Nargis in 2008 (52), natural expansion of mangroves on newly formed mudbanks (particularly in Tanintharyi), a national mangrove logging ban passed in 2014 (53) and legal frameworks for community management (51), passive natural regeneration in abandoned areas, and active plantation and restoration efforts (54).

Beyond mapping areal change, this work provides spatially explicit annual data on global mangrove canopy density extending back to the 1980s, enabling continuous monitoring of global mangrove degradation growth. Distinguishing between mangrove degradation and loss is critical, as they could be driven by different processes, have distinct ecological consequences, and require tailored conservation strategies (20). Our long-term record of canopy density reveals that mangrove degradation, particularly following tropical cyclones, affects a much larger area than loss in certain years. It also captures the non-linear dynamics (e.g., and subsequent decline) of loss rates in Southeast Asia (Fig. 4B), highlighting fine-scale temporal variation in mangrove disturbance. Importantly, we found that persistent mangrove stands can increase in canopy density by closing internal gaps, a dynamic largely overlooked in extent-based observations. The expansion of closed-canopy forests enhances sediment trapping and could serve as the seed sources for facilitating propagule dispersal, promoting resilience to sea-level rise and supporting lateral expansion (55), suggesting a positive-feedback mechanism in mangrove development. Moreover, increases in canopy density without associated land-cover change imply net biomass accumulation and carbon storage. These findings indicate that assessments of blue carbon dynamics based solely on areal extent (56) may underestimate carbon gains, particularly where structural canopy changes are not accounted for. However, it is important to note that newly formed closed-canopy mangrove stands are not necessarily equivalent to mature forests. Younger stands may provide reduced ecological services relative to the older, deforested mangroves (57). As such, offsetting functional losses from deforestation through mangrove gain requires not only spatial compensation but also sufficient time for ecosystem maturation and full functional recovery.

Our findings provide useful insights for future policy and research. Conservation efforts should prioritize halting deforestation, as mangroves exhibit a natural capacity for gaining and growing once pressures are controlled. Crucially, conservation frameworks must look beyond area-based targets alone. Gains in canopy density, such as transitions from open to closed mangrove forest, enhance ecological functioning including increased carbon storage, which in some instances may outweigh carbon emissions from losses of sparse mangrove forests. Newly established mangrove stands warrant particular attention. Understanding the mechanisms underpinning their expansion is essential for guiding restoration strategies and optimizing their carbon sequestration potential. These young forests represent a substantial and growing carbon sink (58) but may be more sensitive to cyclones due to underdeveloped trunks and anchoring root systems. Conservation policy, therefore, should give more emphasis on protecting those naturally generated mangrove forests rather than solely focus on mangrove planting.

In summary, our study provides the first spatially explicit global-scale measurement of mangrove loss, gain (including expansion and regeneration), degradation, and growth at an annual frequency. We reveal that global mangrove losses since the 1980s have been largely offset by widespread but previously undetected expansion and regeneration, resulting in only a marginal net decline in extent by 2023. With both loss and degradation rates declining in recent years, mangroves have shifted to a trajectory of net gain since 2010. This reversal, however, should not be seen as grounds for complacency. Rather, it highlights the substantial conservation potential of halting deforestation and supporting regrowth, given the demonstrated capacity of mangroves to expand and thrive. Our findings thus offer a new basis for understanding and predicting mangrove dynamics, advancing global ecosystem restoration goals, and refining strategies to mitigate climate change through blue carbon ecosystems.

REFERENCES AND NOTES

291

292

293

294

295

296

297

298

299

300

301

302

303

304

305 306

307

308 309

310

311

312

313

314

315 316

318

320

322

323

324

325

326

327 328

330

331

332

333

335

336

337

338

339

340

341

342

343

344

345

346

- 1. C. Fu, A. Steckbauer, H. Mann, C. M. Duarte, *Nat. Rev. Earth Environ.* 5, 538–552 (2024).
- 2. Q. He et al., Nat. Rev. Biodivers. 1, 50-67 (2025).
- 3. P. I. Macreadie et al., Nat. Rev. Earth Environ. 2, 826–839 (2021).
- 4. C. A. Buelow et al., Curr. Biol. 32, 1641-1649.e3 (2022).
- 5. S. Y. Lee et al., Glob. Ecol. Biogeogr. 23, 726–743 (2014).
- 6. L. Goldberg, D. Lagomasino, N. Thomas, T. Fatoyinbo, Glob. Change Biol. 26, 5844–5855 (2020).
- 7. D. R. Richards, D. A. Friess, *Proc. Natl. Acad. Sci.* **113**, 344–349 (2016).
- 8. Y. Jiang et al., One Earth. 8, 101149 (2025).
- 9. D. Lagomasino et al., Nat. Commun. 12, 4003 (2021).
- 10. Z. Zhang, M. R. Ahmed, Q. Zhang, Y. Li, Y. Li, Remote Sens. 15, 625 (2023).
 - 11. N. J. Murray et al., Science. 376, 744–749 (2022).
- 12. P. Bunting et al., Remote Sens. 14, 3657 (2022).
 - 13. S. D. Sasmito et al., Nat. Ecol. Evol. 7, 62–70 (2023).
- 14. T. A. Waleed, Y. K. Abdel-Maksoud, R. S. Kanwar, H. Sewilam, *Int. J. Environ. Sci. Technol.* **22**, 1225–1262 (2025).
- 15. X. Wang et al., Nat. Sustain. 4, 1076–1083 (2021).
- 16. J. H. Nienhuis et al., Nature. 577, 514-518 (2020).
- 17. Z. Dai, C. Long, X. Mei, S. Fagherazzi, Y. Xiong, Geophys. Res. Lett. 51, e2024GL109675 (2024).
- 18. J. Peereman, J. A. Hogan, T.-C. Lin, *Glob. Ecol. Biogeogr.* **31**, 37–50 (2022).
- 19. Z. Zhang, X. Luo, D. A. Friess, Y. Li, Nat. Geosci. 18, 488-494 (2025).
- 20. D. A. Friess et al., Annu. Rev. Environ. Resour. 44, 89–115 (2019).
- 21. E. S. Yando et al., Biol. Conserv. 263, 109355 (2021).
- 22. L. Carugati et al., Sci. Rep. 8, 13298 (2018).
 - 23. D. Reed et al., Glob. Change Biol. 31, e70124 (2025).
- 24. L. Lymburner et al., Remote Sens. Environ. 238, 111185 (2020).
- 317 25. S. Wei, H. Zhang, J. Ling, GIScience Remote Sens. **62**, 2491920 (2025).
 - 26. C. Vancutsem et al., Sci. Adv. 7, eabe1603 (2021).
- 319 27. Y. Liu et al., Sci. Data. 11, 832 (2024).
 - 28. T. T. Caughlin, S. W. Rifai, S. J. Graves, G. P. Asner, S. A. Bohlman, Remote Sens. Ecol. Conserv. 2, 190-203
- 321 (2016).
 - 29. E. J. Anthony et al., Earth-Sci. Rev. 103, 99–121 (2010).
 - 30. C. Proisy et al., Cont. Shelf Res. 29, 632–641 (2009).
 - 31. E. N. Dethier et al., Nature. 620, 787–793 (2023).
 - 32. J. O'Farrell et al., Remote Sens. 17, 358 (2025).
 - 33. V. Hagger et al., Nat. Commun. 13, 6373 (2022).
 - 34. R. Bardou, D. A. Friess, T. W. Gillespie, K. C. Cavanaugh, Glob. Ecol. Conserv. 53, e03022 (2024).
 - 35. S. S. Chand et al., Nat. Clim. Change. 12, 655–661 (2022).
- 329 36. H. C. Teo et al., Nat. Sustain. **8**, 358–362 (2025).
 - 37. E. Monga, M. M. Mangora, J. S. Mayunga, West. Indian Ocean J. Mar. Sci. 17, 1–10 (2018).
 - 38. N. Saintilan, N. C. Wilson, K. Rogers, A. Rajkaran, K. W. Krauss, Glob. Change Biol. 20, 147–157 (2014).
 - 39. M. Jia, Z. Wang, Y. Zhang, D. Mao, C. Wang, Int. J. Appl. Earth Obs. Geoinformation. 73, 535–545 (2018).
 - 40. L. Ruan, M. Yan, L. Zhang, X. Fan, H. Yang, Sci. Total Environ. 844, 157075 (2022).
- 334 41. Z. Zhang et al., Nat. Ecol. Evol. 8, 239–250 (2024).
 - 42. J. Andrieu et al., For. Ecol. Manag. 461, 117963 (2020).
 - 43. G. T. Vanin, E. R. Lacerda, G. M. Mori, Conserv. Biol. 39, e14426 (2025).
 - 44. H. Almahasheer, A. Aljowair, C. M. Duarte, X. Irigoien, Estuar. Coast. Shelf Sci. 169, 164–172 (2016).
 - 45. M. Mohan et al., Remote Sens. Appl. Soc. Environ. 36, 101345 (2024).
 - 46. Y. Xia, K. Liu, Y. Zhu, X. Wen, J. Cao, Environ. Monit. Assess. 197, 762 (2025).
 - 47. E. Dutrieux *et al.*, (https://dx.doi.org/10.2118/168449-MS).
 - 48. P. P. Thant et al., Mar. Environ. Res., 107343 (2025).
 - 49. K. Win, J. Sasaki, Remote Sens. 16, 4077 (2024).
 - 50. V. B. Arifanti et al., Forests. 13, 695 (2022).
 - 51. L. Slobodian et al., Cell Rep. Sustain. 2 (2025).
 - 52. T. T. Aung, Y. Mochida, M. M. Than, For. Ecol. Manag. 293, 103–113 (2013).
 - 53. G. W. Prescott et al., Conserv. Biol. 31, 1257–1270 (2017).
 - 54. W. M. Aye, S. Takeda, *Paddy Water Environ.* **18**, 417–429 (2020).
- 55. M. P. Kumara, L. P. Jayatissa, K. W. Krauss, D. H. Phillips, M. Huxham, *Oecologia*. **164**, 545–553 (2010).

- 56. S. E. Hamilton, D. A. Friess, *Nat. Clim. Change.* **8**, 240–244 (2018).
- 57. S. Y. Lee, S. Hamilton, E. B. Barbier, J. Primavera, R. R. Lewis, *Nat. Ecol. Evol.* 3, 870–872 (2019).
- 58. N. Robinson et al., Nat. Clim. Change. 15, 793–800 (2025).

ACKNOWLEDGMENTS

349

350

351

352 353

354

355

356

357

358

359

360 361

362

363 364

365

366

367

368

369

370

371

372

373

374

375

376 377

378

379

We thank the School of Science and Engineering of Tulane University for general support and L. Lamb-Wotton and Z. Shribman at the Mangrove Lab for assisting PlanetScope satellite data processing. Funding: This work was supported by grants from the Cochran Family Professorship in Earth and Environmental Sciences at Tulane University (to D.A.F.), which was endowed by Michael and Mathilda Cochran. Author contributions: Z.Z. conceived the study, developed the mangrove dynamic dataset, designed and performed the analysis, and wrote the original draft of the paper. D.A.F. contributed supervision, funding, experimental design, research questions and draft writing. X.P.S contributed to the design of the validation procedure. P.B. validated our results by comparing with the ongoing Global Mangrove Watch v4.0 change dataset. V.B.A, T.T.A, and S.S.H provided local experience in Indonesia and Myanmar for validating our findings. All authors commented on and edited the final version of the manuscript. Competing interests: The authors declare that they have no competing interests. **Data and materials availability:** All data used in this study is publicly available. Existing global-scale mangrove datasets used in this study can be accessed here: the Global Mangrove Watch (https://zenodo.org/record/6894273), the High-resolution Global Mangrove Forests (https://dataverse.harvard.edu/dataset.xhtml?persistentId=doi:10.7910/DVN/PKAN93), the ESA global mangrove (https://worldcover2020.esa.int/), the Global Mangrove Forest Distribution in 2020 in 2000 (https://developers.google.com/earth-engine/datasets/catalog/LANDSAT MANGROVE FORESTS), and the Global Wetland Layer FCS30D (https://zenodo.org/records/10068479). Satellite data from Landsat 4, 5, 7, 8, and 9 are freely available from the GEE platform. PlanetScope SuperDove images used in validating our FCC data were obtained through the Planet Labs' Education and Research Program, which allowed for free-of-charge downloads of a maximum 3,000 km² per month. Our generated global mangrove dynamic data are available at Zenodo (https://zenodo.org/communities/cgmd/) and be can accessed https://zhenzhang.users.earthengine.app/view/globalmangrovedynamic. Python code for graphics and analyses is available on GitHub at https://github.com/GIS-ZhangZhen/ContinuousGlobalMangroveDynamics.

Supplementary Materials

- Materials and Methods
- Figs. S1 to S24
- Tables S1 to S6
- 381 References (59–118)

Materials and Methods

Generation of Landsat baseline imagery.

The entire archive of the Landsat Collection 2 Tier 1 surface reflectance images (1) acquired between 1984 and 2023 was used to generate the mangrove extent and Fractional Canopy Cover data. Cloud and cloud shadows in the Landsat images were masked out using the Quality Assessment (QA) information on the Google Earth Engine (GEE) platform (2). To define the study area (fig. S2), we generated a 1° global grid and retained only those cells intersecting with any of five existing global mangrove datasets, including Global Mangrove Watch (GMW v3, 1996-2020) (3), the High-resolution Global Mangrove Forests in 2020 (HGMF_2020) (4), the Global Mangrove Forest Distribution in 2000 (GMFD_2000) (5), the ESA global mangrove extent in 2020 (ESA_2020) (6), and the Global Wetland Layer FCS30D (GWL_FCS30D, 2000–2020) (7).

Due to the uneven Landsat coverage, especially prior to the launch of Landsat 7 in 1999, generating global annual mangrove extent maps and associated dynamics posed a challenge. We thus adopted a grid-specific mosaicking strategy to generate cloud- and gap-free baseline composites for three anchor years: 1984 ("1980s baseline"), 2010, and 2023, which served as temporal benchmarks for subsequent mangrove mapping and change detection. Each baseline image was initialized with imagery from its target year and iteratively gap-filled using median annual composites from adjacent years until complete coverage was achieved. The initial year of valid Landsat observations for the 1980s baseline varied regionally due to differences in sensor acquisition coverage (fig. S14 and fig. S15), but 97% of pixels were acquired between 1984 and 1989 (fig. S16), supporting its representation of the "1980s" composite. Valid initial observations began in 1984 for most of the Americas, Africa, and the Middle East; in 1986 for Australia and East Asia; in 1987 for Southeast Asia; in 1988 for South Asia; and in 1989 for the Pacific Islands. The 2023 composite benefited from Landsat 9 and required only minimal backward extension (January 2023-July 2024) to ensure gap-free coverage.

Producing global annual mangrove fractional canopy cover data.

Fractional canopy cover (FCC), the proportion of vegetation canopy over the ground surface (8), is a commonly used remote sensing index to measure forest degradation (9–11). We estimated FCC using spectral mixture analysis (SMA), which models pixel reflectance as a linear combination of spectral characteristics of pure land-cover types (so-called endmembers, usually including green vegetation and bare soil) (12). To overcome the inefficiency of manually defining endmembers at global scale, we developed an automated method to extract them from each annual Landsat composite. The main strategy was to identify high-purity pixels for each land-cover type and use their mean spectral signatures as endmembers (13). We included water as the third endmember class considering high water content in the coastal area (13). Additionally, the green vegetation class was restricted to pure mangrove vegetation to ensure a more representative spectral signature of mangrove canopies.

To identify the bare soil subset, we excluded water bodies using the Global Surface Water (GSW) maximum extent mask (14), Normalized Difference Water Index (NDWI) (15) < 0, and elevation > 1 m (to eliminate intertidal mudflats which usually hold high soil moisture content), and vegetation using Normalized Difference Vegetation Index (NDVI) (16) < 0.3 and Normalized Difference Built-up Index (NDBI) (17) > 0. We then retained remaining pixels with blue band reflectance below the 30th percentile (18) to exclude bright non-soil surfaces (e.g., sand and impervious surfaces). The remaining areas were treated as the bare soil subset due to their low water and vegetation probability and low spectral reflectance in visible wavelengths (fig. S17). The mangrove vegetation subset was derived by selecting pixels within mapped mangrove extents (see subsequent sections) exceeding the 90th percentile of mangrove NDVI, which represent high-density mangrove canopy areas. The water endmember was obtained from GSW pixels with > 98% water occurrence, representing permanent water bodies (14).

Because FCC is a continuous variable and sensitive to thin clouds, we applied an additional procedure to remove residual cloud contamination from Landsat images after QA-band masking. We observed that clear-sky mangrove pixels consistently exhibit blue band reflectance < 0.07 and shortwave infrared band (SWIR1) reflectance > 0.05 (fig. S18), which were used to enhance cloud and shadow removal for FCC estimation (fig. S18). To generate a seamless FCC product, FCC values for the gap-free 1980s Landsat composite were assigned to 1984, and missing values in subsequent years were filled using the most recent valid FCC observation.

To validate FCC estimates from our unmixing approach, we used high-resolution (3 m) PlanetScope SuperDove imagery over two mangrove sites: the Everglades in the United States and the Herbert Creek Estuary in Australia. At each site, mangrove canopy cover was mapped at 3 m resolution and then aggregated to a 30 m grid to generate reference FCC layers for validating. We compared our SMA-derived FCC estimates against four alternative approaches (19), including a quadratic model based on NDVI:

$$FCC = \left(\frac{NDVI - NDVI_S}{NDVI_v - NDVI_S}\right)^2 \tag{1}$$

where $NDVI_s$ and $NDVI_v$ are the NDVI values of the bare soil and mangrove endmembers, respectively, and relative vegetation abundance (RA) algorithms based on three vegetation indices, namely NDVI, kernel NDVI (kNDVI) (20), and near-infrared reflectance of vegetation (NIRv) (21), each of which was computed using a standard linear unmixing formula:

$$FCC = \frac{VI - VI_S}{VI_v - VI_S} \tag{2}$$

where VI refers to the pixel-level vegetation index (i.e., NDVI, NIRv, or kNDVI), and VI_s and VI_v denote the corresponding values for bare soil and mangrove endmembers, respectively. The FCC estimates derived from our SMA approach exhibited greater stability than alternative methods, with root mean square error (RMSE) ranging from 14% to 18% across two validation sites (fig. S19).

Generating global mangrove baselines.

Automatic training sample collection.

We developed an automated methodology to generate both mangrove and non-mangrove training samples for delineating mangrove extents from the three Landsat baseline composites. We first defined a consensus mangrove extent by intersecting multiple existing global mangrove datasets for the years 2000 (GMFD_2000, GWL_FCS30D_2000, and GMW_1996), 2010 (GMW_2010 and GWL_FCS30D_2010), and 2020 (HGMF_2020, GWL_FCS30D_2020, GMW_2020, and ESA_2020). Considering that even these consensus areas may still contain commission errors, we refined them using Landsat-derived spectral indices. Specifically, for each 1° grid cell, pixels with low values of the logarithm of the Mangrove Vegetation Index (22) (MVI_{log}; < mean – 1 s.d.) and high values of the Modular Mangrove Recognition Index (23) (MMRI; > mean + 1 s.d.) were excluded, as mangroves typically exhibit high MVI_{log} and low (often negative) MMRI. MVI_{log} was preferred over raw MVI due to the latter's wide range (could be greater than 20), which can raise large standard deviations and thus an inaccurate threshold.

Due to the limited availability of multi-source mangrove data, the earliest reliable mangrove intersection could only be established for the year 2000, with the latest being 2020. To transfer the 2000 and 2020 intersected mangrove extents to the 1980s and 2023, we used a metric of spectral similarity called Spectral Angle Mapper (SAM) (24). For example, to derive training data for the 1980s baseline, we calculated SAM between the 1980s and the 2000 Landsat median composites, retaining mangrove pixels with SAM < 0.15 as unchanged mangroves (fig. S20). Mangrove samples were then randomly sampled within the corresponding intersected mangrove extents for the 1980s, 2010, and 2023. To balance computational efficiency and spatial representativeness, mangrove training samples were limited to 20,000 per subregion (approximately three 1° grid cells) per baseline year (fig. S2B).

Non-mangrove training samples were generated by excluding any potential mangrove pixels. To achieve this, we generated a union layer of all existing global mangrove datasets, which was then masked out from its 3-km buffer, leaving the remaining pixels as potential non-mangrove regions. Pixels exhibiting high MVI $_{log}$ or low MMRI values within the remaining areas were filtered out to further exclude potential mangroves. We also excluded potential water or impervious surfaces using NDVI > 0.2 and Modified Normalized Difference Water Index (MNDWI) (25) > -0.1 as they are easily distinguished from mangroves. The remaining non-mangrove samples were therefore more non-mangrove vegetation related and thus could enhance the ability of trained classifiers in distinguishing mangroves with other vegetation types. We also excluded pixels with substantial spectral changes (SAM > 0.15) across the three baseline years to avoid cases where land cover may transfer to mangroves. We then randomly generated up to 50,000 non-mangrove samples for each subregion (fig. S21).

Region-specific mangrove baseline classification.

To enhance accuracy across geographically diverse mangrove habitats, we implemented a regionspecific modelling strategy (26) by training individual Random Forest (RF) (27) classifiers for each subregion (fig. S2B) and each baseline year using GEE. Isolated islands were grouped into a single classification unit or merged with nearby subregions to ensure an adequate training sample size. From the auto-generated samples, 70% were randomly selected for training to avoid overfitting caused by using all available mangrove pixels. On average, each subregion contained approximately $11,757 \pm 4,444$ (standard deviation), $12,346 \pm 3,913$, and $12,421 \pm 3,876$ mangrove samples for the 1980s, 2010, and 2023 baselines, respectively, along with 29.319 ± 11.566 non-mangrove samples. Globally, this yielded approximately 4 million mangrove training points per baseline year and 10 million non-mangrove training points. Predictor variables in the RF classifier include raw Landsat spectral bands, a suite of derived indices, including NDVI, NIRv, MVI, MVIlog, MMRI, MNDWI, NDBI, and the Tasseled Cap Transformation components, and elevation from the Advanced Land Observing Satellite World 3D data. Considering that the spectral characteristics of mangroves change with tide level (28), we generated two quantile composite images (90th and 10th percentiles) for each baseline year for classification (29), which can improve the discrimination between mangrove and terrestrial vegetation (28). Each RF classifier used 200 decision trees, a hyperparameter adopted from previous studies (28, 30) as sufficient to balance computational efficiency and model performance. Outputs from the RF classifier were in a probabilistic mode varying between 0 and 100%, representing the likelihood of each pixel being mangrove. We adopted a strict classification threshold of 95% to minimize commission errors, as justified by the observed probability distribution of mangrove samples (fig. S22). Pixels with NDVI < 0.2 or FCC < 10% (31) were excluded from the final classification.

A post-processing procedure was applied to further reduce commission errors. First, isolated tiny patches were excluded, unless its area > 3 Landsat pixels and intersected with a 100-m buffer of ocean area or its area > 2 Landsat pixels and intersected with the intersection of existing global mangrove layer. Ocean areas in each subregion were mapped using the GSW permanent water layer for the corresponding year, supplemented by a Landsat-derived water mask (MNDWI > 0, NDWI > 0, or Automated Water Extraction Index (AWEI) (32) > -0.18) and further constrained to low elevations (< 5 m) (fig. S23). To reduce omission errors, we restored pixels from the intersection of existing global mangrove layers showing strong mangrove signals (MVI > 4 and NDVI > 0.3).

Detecting mangrove dynamics and annual extents.

Mangrove change detection between baseline years.

As the three mangrove baselines (1980s, 2010, and 2023) were generated independently, direct postclassification comparison would lead to error propagation as differences between maps may reflect varying accuracies rather than true changes (33). To address this, we developed a spectral differencing framework that integrates changes in the Spectral Angle Mapper (SAM) and Mangrove Vegetation Index (MVI) to identify true mangrove changes and refine baseline extents. The key to our approach is built upon the concept that true mangrove change, whether loss or gain, is accompanied by substantial spectral variation and the disappearance or emergence of mangrove signals (34). SAM was used to quantify spectral variation, while MVI captured changes in mangrove features.

For the 1980s-2010 comparison, pixels labeled as mangrove in the 1980s but non-mangrove in 2010 were considered loss candidates. A SAM between the two Landsat baseline composites exceeding 0.3 was sufficient to confirm spectral variation (fig. S20). For intermediate SAM values (0.15-0.3), we confirmed them as true mangrove loss only if they have a large MVI drop (> 2) and small mangrove signal in 2010 (MVI_{log} below mean - 1 s.d. of persistent mangrove pixels). Gain detection followed an inverted logic, requiring increased MVI (i.e., increased mangrove signal), high SAM (substantial spectral variation), and low 1980s MVI_{log} (non-mangrove in the start year so the increased mangrove signal represents a mangrove gain). Stable mangrove areas were defined as the persistent mangrove pixels between baseline years, as well as those false change pixels with majority agreement among the three classifications. The 1980s baseline was updated by combining confirmed loss and stable areas; similarly, the updated 2010 baseline confirmed gain and stable mangroves.

The same procedure was applied to the 2010-2023 period. Since the 2010 baseline was refined from both comparisons, two updated versions were generated. In overlapping zones, the shared classification was retained; in inconsistent areas, only pixels with MVI>4 were preserved as mangrove to ensure reliability. As the baseline 2010 was updated, the change layers were also slightly altered. To reduce false positives, tiny change patches (< 3 Landsat pixels) were excluded as false changes and were reclassified based on the classification majority across the three baselines. Through this change detection and correction process, we refined the three global mangrove baselines and generated corresponding loss and gain layers.

Depicting the annual mangrove extent and dynamics.

For each mangrove change pixel, the year of change was determined using a minimum variance segmentation approach (35):

$$D = min(\sum_{i=1}^{h-1} (x_i - mean([x_1, ..., x_{h-1}]))^2 + \sum_{i=h}^{n} (x_i - mean([x_h, ..., x_n]))^2) (3),$$

where D represents the minimum variance among all variances, x represents the MVI_{log} time series, n is the number of annual observations, and h is the candidate change year. The year h that minimized the sum of within-segment variances was identified as the change year. For loss pixels, years before h were labeled as mangrove and after as non-mangrove; the reverse applied to gain pixels. These temporal classifications, combined with stable mangrove areas, formed annual mangrove extents. Considering that change can happen multiple times and even stable mangroves can also change in the intervening years, we excluded pixels with low vegetation probability (NDVI < 0.2 or FCC < 10%) from annual mangrove extents. Missing data caused by cloud contamination or lacking images were gap-filled using the previous year's classification. Further, short-term changes (< 3 years) are mostly noise-induced spikes so were corrected as stable to improve temporal consistency (36, 37), forming a continuous annual mangrove extent dataset with change information.

Mangrove dynamics were then extracted, distinguishing structural changes (degradation/growth) from categorical changes (loss/gain). Each annual extent map was stratified into four canopy cover classes: closed mangrove forest (FCC > 80%), open mangrove forest (50%-80%), mangrove woodland (20%-50%), and sparse mangrove (< 20%) (38). Degradation was identified as a downward transition (e.g., closed to open), with a > 20% decline in FCC and > 0.15 NDVI drop; growth as the inverse. We detected both abrupt and gradual degradation (e.g., decade-long shifts from closed to open canopy) by comparing the canopy condition of each pixel in the first year against subsequent years until a degradation was observed. Due to the temporal consistency correction, short-term mangrove loss (< 3 years) would be detected as degradation if it is

associated with a substantial FCC drop, distinguishing them from real loss. Notice that for years after 2021, such short-term losses may be classified as real losses due to insufficient post-event observations.

Estimating annual rate of mangrove loss and degradation.

Data gaps in annual Landsat composites can lead to underestimation of observed annual mangrove loss and degradation. To address this, we developed a machine learning-based approach to estimate the actual annual area of mangrove loss and degradation at the regional scale.

We first calculated the valid mangrove area ratio for each year, the proportion of mangrove area derived from valid (i.e., non-gap-filled) Landsat pixels relative to the total mangrove extent (after gap filling), as well as annual observed loss and degradation rates. For years with valid mangrove area ratios > 60%, we assumed the observed change rates were representative of the full mangrove extent, then the actual loss and degradation areas were estimated by multiplying the observed rates by the total mangrove area that year.

For years with a valid mangrove area ratio below 60%, this assumption may no longer hold due to insufficient observational coverage. To estimate actual changes for these years, we trained a time-series XGBoost model (39), a gradient-boosted decision tree method known for its performance in temporal prediction. The model was fitted using the estimated loss and degradation areas (i.e., from years with valid ratios > 60%) as the response variable, along with predictors including year, valid mangrove area ratio, total gap-filled mangrove area, observed mangrove area, observed loss or degradation area, and the lag-1 value of the response variable. Hyperparameters were optimized via a grid search, resulting in a final model with 90 trees, learning rate of 0.2, maximum depth of 3, and subsample rate of 0.7. Model performance was evaluated using leave-one-out cross validation (table S2), demonstrating robust inference of mangrove loss and degradation rates for data-lacking years.

Validation

Sampling design.

We employed a stratified random sampling design, following established 'good practice' (40), to estimate both accuracy and sample-based area of our mangrove change maps across the three epochs (1980s-2010, 2010–2023, and an intervening epoch 1996–2020). Sample size was determined as 998 per epoch using Eq. (13) in ref.(40) with the expected standard error of overall accuracy setting as 0.01, and then tripled to 2,994 per epoch (8,982 in total) to enhance reliability. We also conducted a sensitivity analysis on the changes of accuracy with validation sample size, which shows that 2,994 samples are sufficient for obtaining robust validation results (fig. S24). Sample units were distributed proportionally across strata defined by change-map classes (loss, gain, stable mangroves, and stable non-mangroves) and the ten biogeographic regions (fig. S2A). Because loss and gain were our target classes but represented smaller fractions compared to the stable classes, we upweighted the change classes, allocating 40% of validation sample to loss and gain and 60% to the stable classes89. This ensured that overall accuracy was not disproportionately influenced by the typically higher accuracies of stable categories. To measure omission errors, we generated stable non-mangrove samples from the 1-km buffer surrounding the union of loss, gain, and stable mangrove classes for each epoch, after removing the union itself. Within this spatial buffer, consistent water bodies were excluded because they have a very low probability of containing omitted mangroves but would dominate the random sampling due to their large area. The validation sample was then randomly generated within each change class in each biogeographic region.

Response design.

We labelled each sample unit at the Landsat pixel level. Reference classes for each random pixel were assigned using high-resolution Google Earth imagery whenever available, 30-m Landsat false-color composites, and 10-m Sentinel-2 false-color imagery for the corresponding epoch. Sample pixels were

interpreted independently in a blind manner, with an interpreter unaware of their mapped class labels or strata. In addition, a Landsat MVI time series (1984-2023) was used to verify whether changes had occurred, which was particularly valuable for cases difficult to interpret from imagery alone (e.g., pre-2000) by inferring from image-abundant years and temporal trajectories. For sample pixels with low confidence in labelling, we cross-checked against existing global mangrove maps and assigned the final class by majority vote.

Accuracy assessment.

By comparing the agreement between the reference label and mapped class, we established an error matrix for each epoch. Since the reference of change classes includes the information of mangrove extent (for example, a mangrove loss pixel during 1980s-2010 means this pixel was mangrove in 1980s but non-mangrove in 2020), we also established an error matrix for each of five years in epochs (i.e., 1980s, 1996, 2010, 2020, 2023) to assess accuracy of our mangrove extent maps. We then reported area-weighted accuracy metrics including user's accuracy (UA), producer's accuracy (PA), and overall accuracy (OA), as well as their associated 95% confidence intervals determined by Eq. (5-7) in ref.(40).

Our change maps and extent maps both show high OA at 96% $\pm 0.7\%$ (95% confidence interval) (table S3). For mangrove losses, our UAs are $86.3\% \pm 2.8\%$, $83.6\% \pm 3.0\%$, and $75.8\% \pm 3.5\%$, and our PAs are $83.7\% \pm 10.1\%$, $78.4\% \pm 9.5\%$, and $85.2\% \pm 11.1\%$ for the 1980s-2010, 1996-2020, and 2010-2023, respectively; for mangrove gains, our UAs are $80.6\% \pm 3.2\%$, $78.2\% \pm 3.4\%$, and $85.0\% \pm 2.9\%$, and our PAs are $77.6\% \pm 9.0\%$, $70.8\% \pm 12.2\%$, and $91.2\% \pm 7.7\%$ for the 1980s-2010, 1996-2020, and 2010-2023, respectively.

Area estimation.

We report areas using two complementary approaches: map-based (3, 34) and sample-based (40). In the map-based approach, we bootstrap the validation sample set to obtain 95th-percentile commission and omission errors, which were then used to derive conservative bounds for both extent and change (3, 34). Further methodological details are available in the Supplementary Information of ref.(34). In the sample-based approach, area estimates were calculated by multiplying the total study area by the weighted sample proportions, with 95% confidence intervals computed as the estimated area $\pm 1.96 \times \text{standard error}$ (40). Net change bounds were derived by bootstrapping the difference between gains and losses, with the 95% confidence interval defined as the 2.5th to 97.5th percentiles of the bootstrapped distribution. Across our datasets, map-based intervals were generally wider and encompassed the sample-based intervals. Accordingly, we mainly report map-based estimates and intervals in the main text but also include the corresponding sample-based point estimates and confidence intervals in table S1.

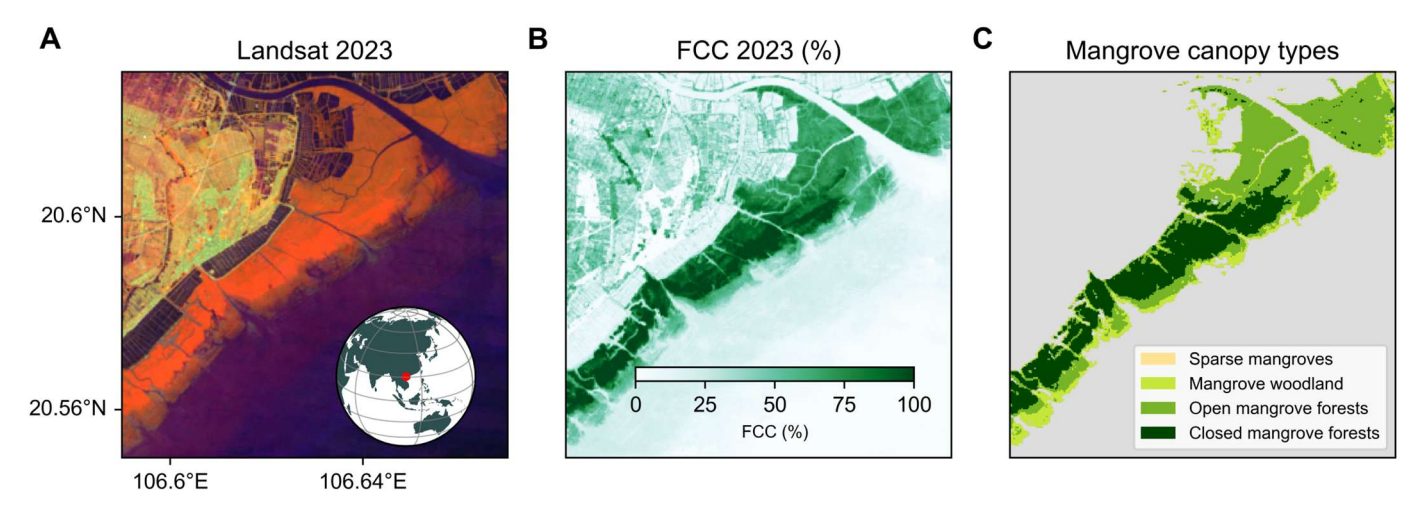
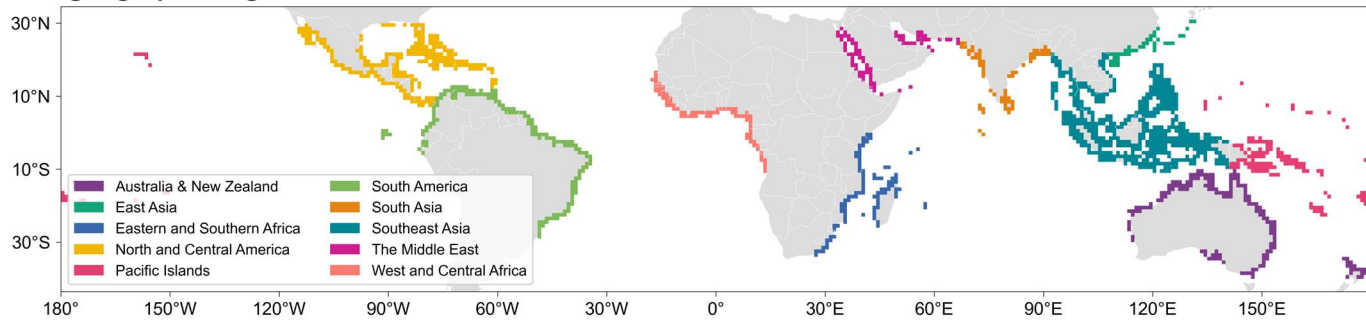


Fig. S1. Derivation of mangrove canopy types from Landsat imagery. **A**, Landsat 2023 composite image of the example area in Vietnam. The inset globe indicates the geographic location of this example site. **B**, Fractional Canopy Cover (FCC) map for 2023, derived from the Landsat imagery shown in panel **A**. The color bar indicates FCC percentages, ranging from 0% (lightest green) to 100% (darkest green). **C**, Reclassified mangrove canopy types based on the FCC data. Categories include Sparse mangroves (FCC < 20%), Mangrove woodland (20%-50%), Open mangrove forests (50%-80%), and Closed mangrove forests (> 80%).

A. Biogeographic regions



B. Classification units

272

273

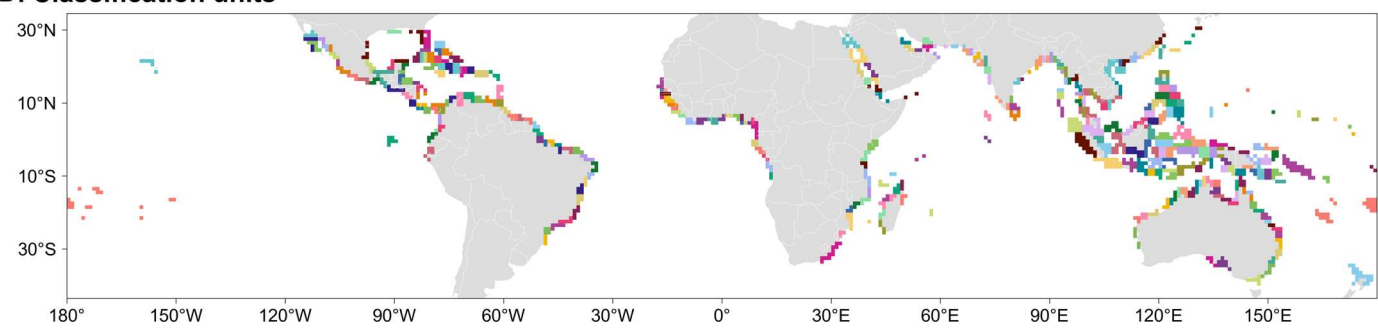


Fig. S2. Spatial units used for mangrove change analysis and reporting. A, Global mangrove extent grouped into ten major biogeographic regions. The color-coding corresponds to the legend, which lists the regions used for regional analysis and reporting. B, Subdivision of the global mangrove extent into finer classification units. These units served as the base spatial units for mangrove mapping and change detection.

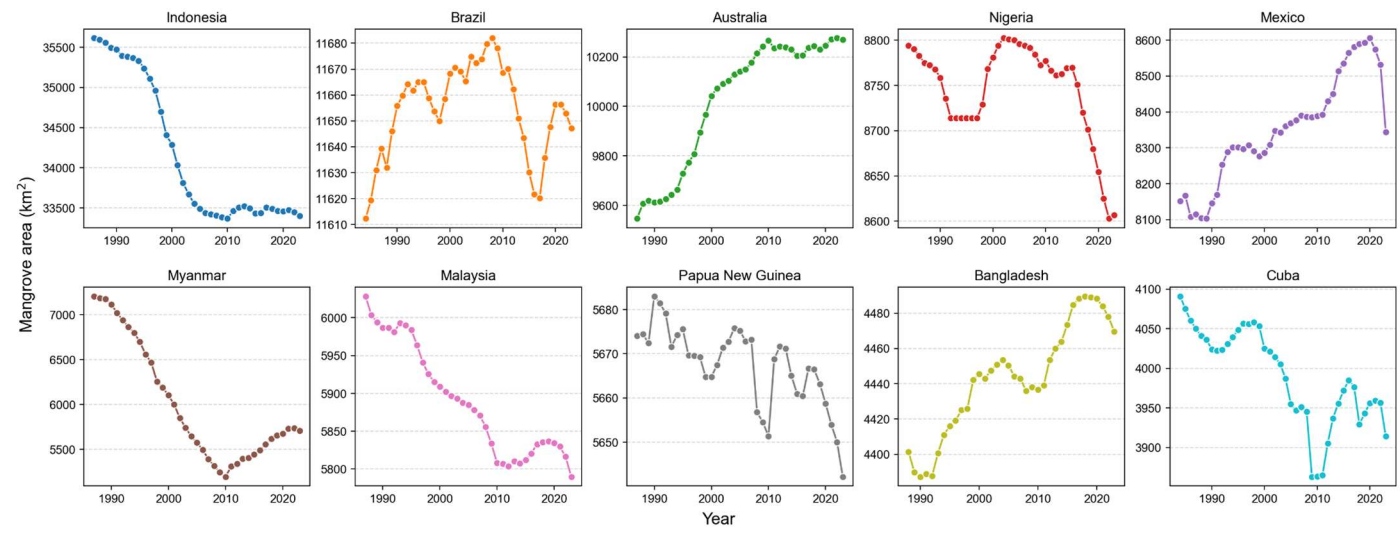


Fig. S3. Temporal dynamics of mangrove area in the ten major mangrove-holding countries. Time series plots illustrate the changes in mangrove area (km²) from the late 1980s to 2023 for the ten countries with the largest mangrove extent during the 1980s. Countries are ordered from left to right, top to bottom, according to their respective mangrove area in the 1980s. The mangrove area decline in Mexico and Cuba after 2021 are primarily attributed to hurricane-induced degradation events; while such short-term events should be classified as degradation upon confirmed recovery, they are currently mapped as deforestation due to the absence of sufficient post-2023 observations to ascertain their recovery.

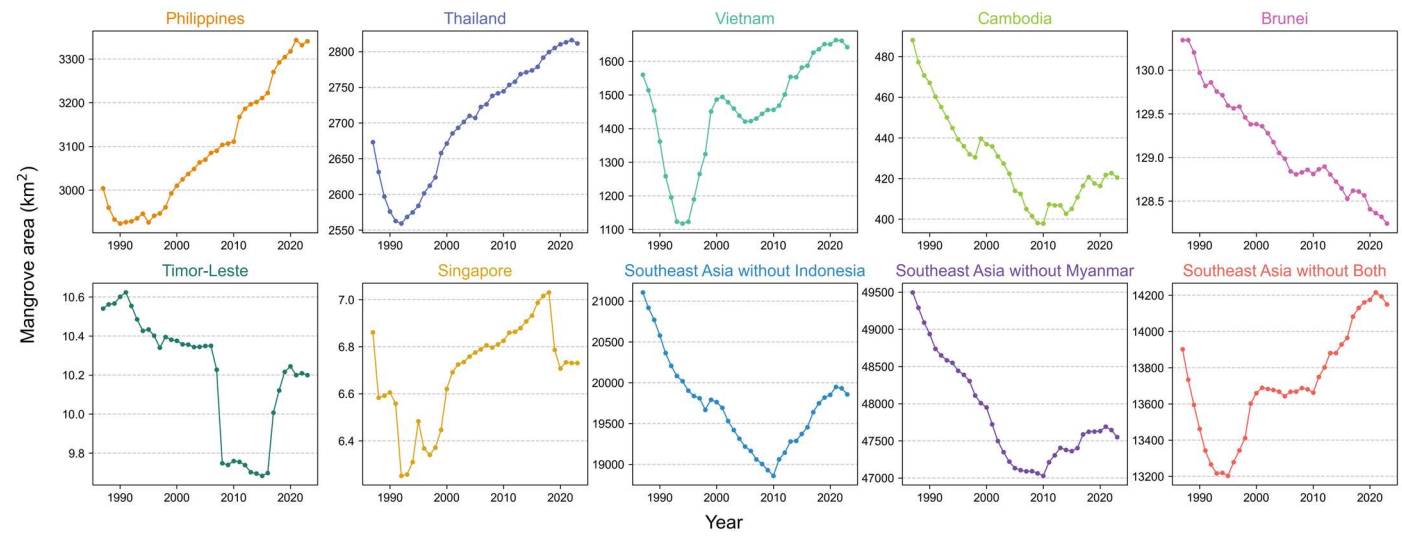


Fig. S4. Mangrove area time series in Southeast Asian countries. Time series plots illustrate the changes in mangrove area (km²) from 1987 to 2023 for Southeast Asian countries. Data for Indonesia, Myanmar, and Malaysia, which are among the top mangrove countries, are presented in Fig. S3. The bottom row's rightmost three panels display the total mangrove area for Southeast Asia when excluding Indonesia, excluding Myanmar, and excluding both Indonesia and Myanmar, respectively, which highlight that the dynamics of mangrove area in Indonesia and Myanmar dominate the overall regional reversal observed around 2010.

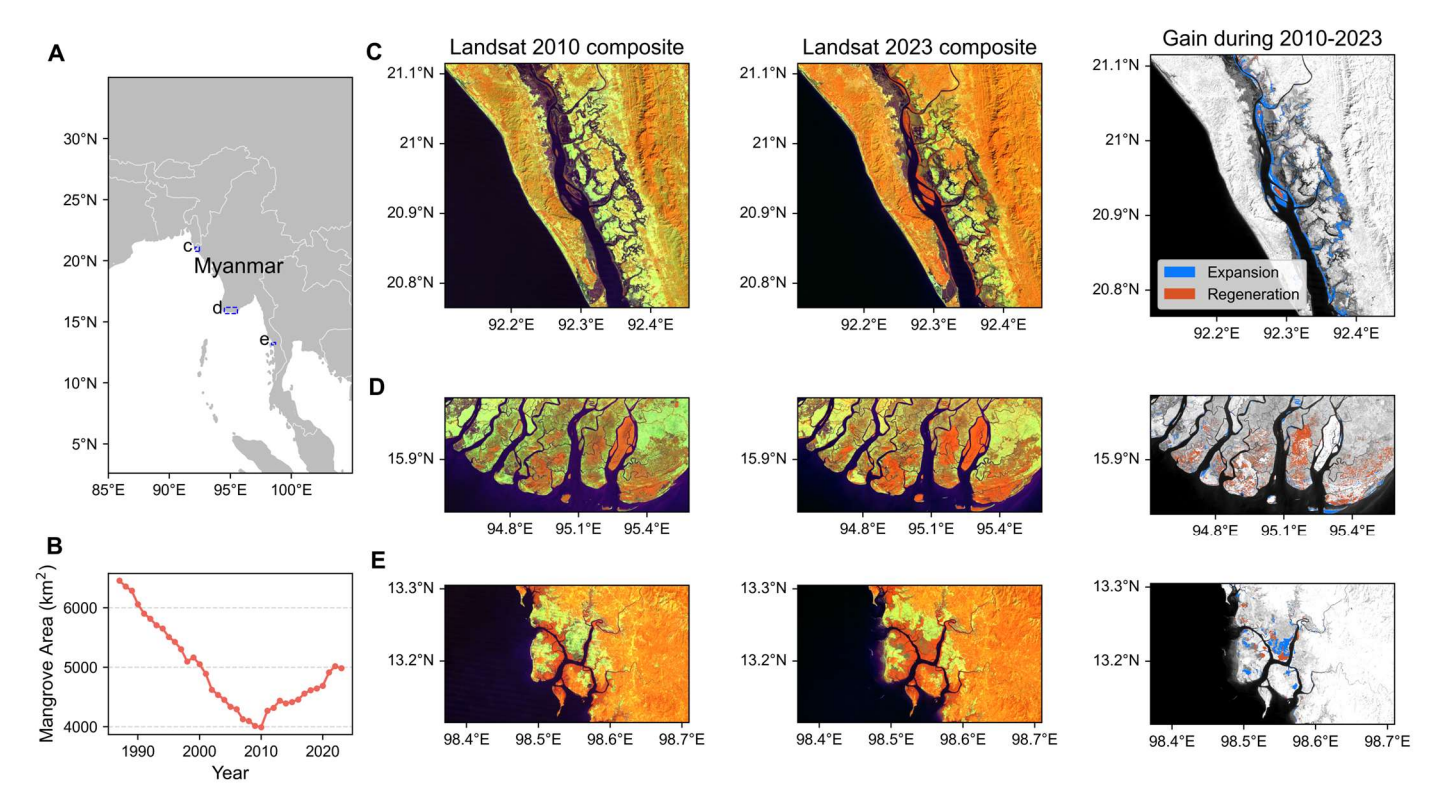


Fig. S5. Mangrove dynamics and gain examples in Myanmar (1987-2023). A, Location map of Myanmar, with blue boxes indicating the regions highlighted in panels C, D, and E. B, Time series of mangrove area (km²) in Myanmar from 1987 to 2023. This time series was generated using a thresholding method where the maximum mangrove area was defined by the union of baseline extents from the 1980s, 2010, and 2023. Annual area updates were determined by applying thresholds of Normalized Difference Vegetation Index (NDVI) > 0.4 and Mangrove Vegetation Index (MVI) > 3.5. This method identifies a similar reversal in the mangrove area around 2010, providing evidence for the robustness of our change detection approach. **C**, **D**, and **E**, Regional examples of mangrove expansion in Myanmar. Each row displays a Landsat 2010 composite (left), a Landsat 2023 composite (middle), and the corresponding mangrove gain map for 2010-2023 (right). Expansion is shown in blue, and regeneration in red. Panel **C** focuses on the Nef River, showing substantial natural riverine expansion. Panel **D** and **E** illustrates the Irrawaddy Delta and the Pyin Bu Gyi Island, where both expansion and regeneration occurred.

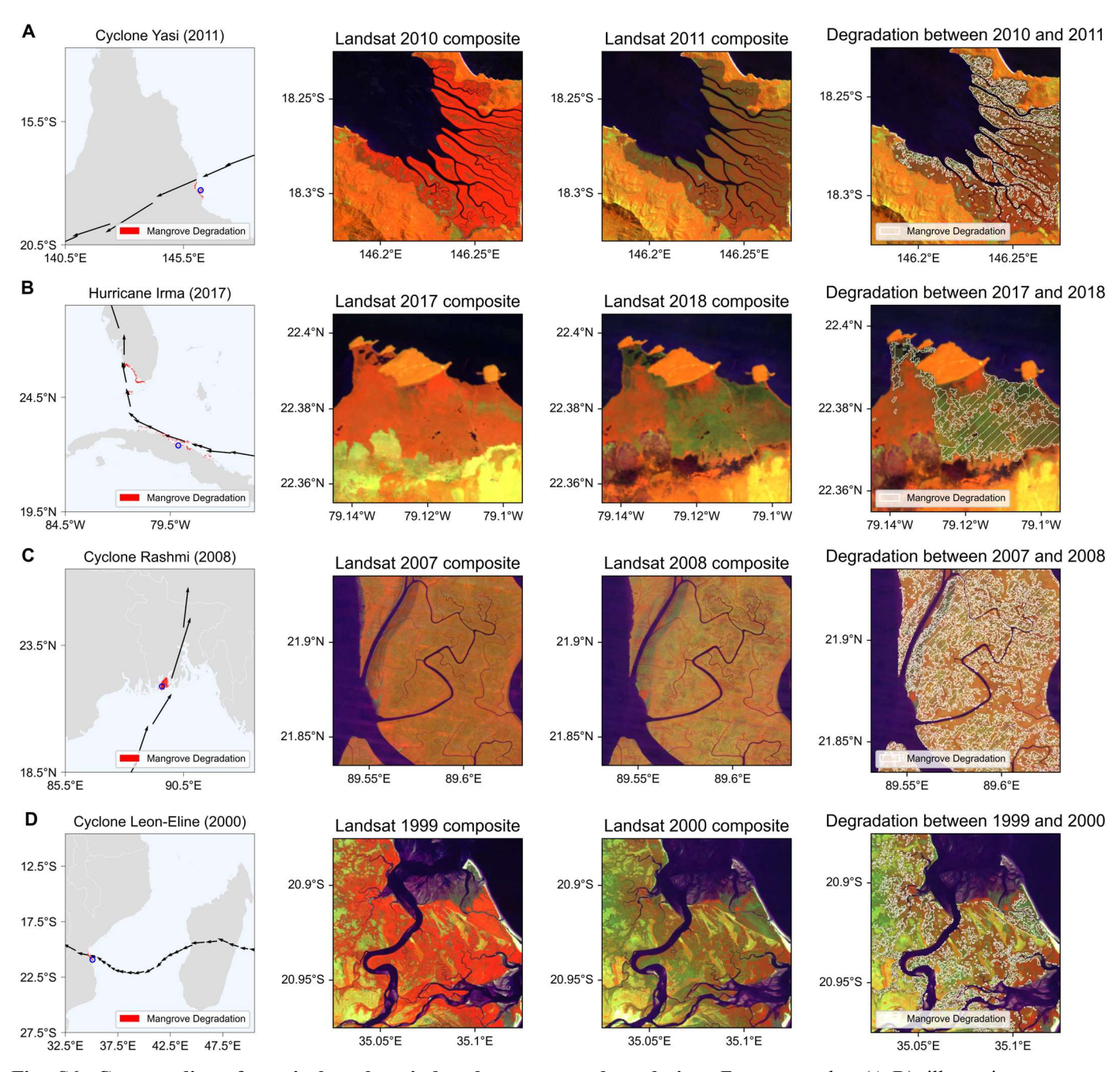


Fig. S6. Case studies of tropical cyclone-induced mangrove degradation. Four examples (A-D) illustrating mangrove degradation events caused by tropical cyclones. For each event, the leftmost column displays the cyclone's path (the black arrows) and the location of mangrove degradation (red shaded area), visibly demonstrating that mangrove degradation areas closely follow the cyclone path. The cyclone paths are derived from the International Best Track Archive for Climate Stewardship (IBTrACS) archive. The blue circles in the left panels indicate the extent of the Landsat imagery shown in the other columns. The second column presents the Landsat composite image acquired before the cyclone event, and the third column shows the Landsat composite image acquired after the cyclone event. The rightmost column provides a view of the mangrove degradation area (white hatched area) on the Landsat image taken after the cyclone.

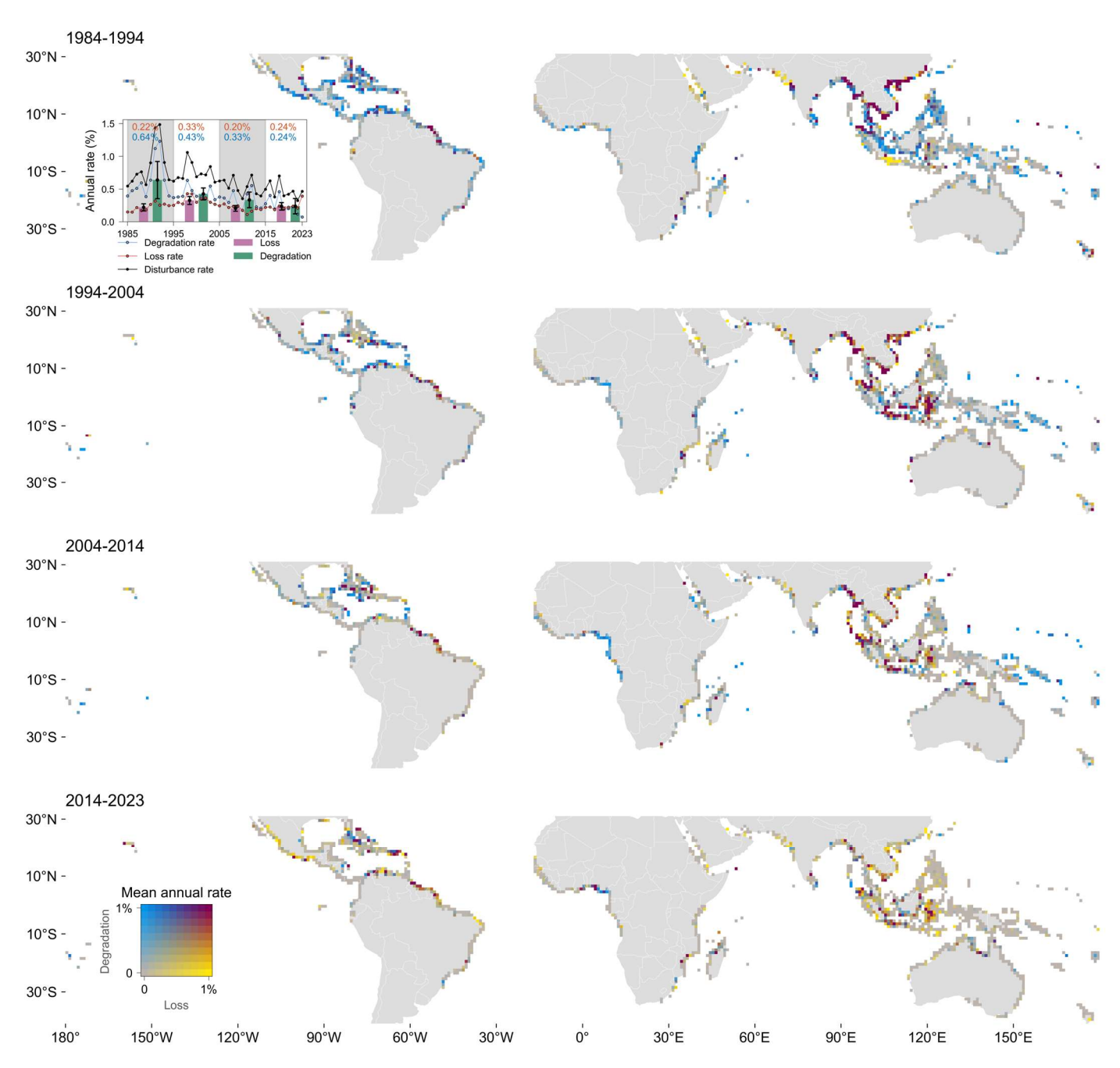


Fig. S7. Decadal dynamics of global mangrove disturbance rates (1984–2023). The evolution of global mangrove loss and degradation rates across four consecutive decadal periods were illustrated: 1984-1994, 1994-2004, 2004-2014, and 2014-2023. Blue hues represent areas where degradation rates are greater than loss rates, while yellow hues represent areas where loss rates are greater than degradation rates; grey indicates low rates for both. A clear global pattern emerges, showing a transition from predominantly blue-dominated areas in earlier decades to increasingly yellow-dominated areas in more recent decades, indicating a global shift towards loss rates surpassing degradation rates.

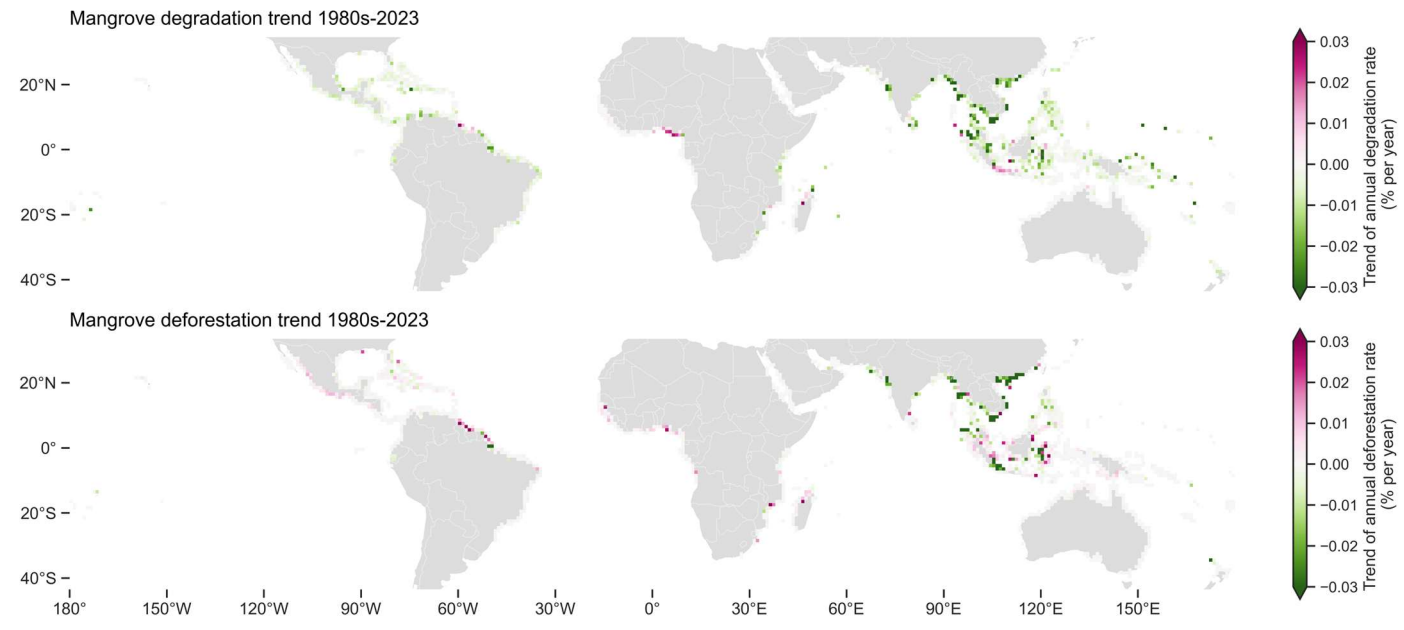


Fig. S8. Global trends in mangrove degradation and loss rates (1980s–2023). For both maps, the trend value for each grid cell was determined using the Theil-Sen slope. The color scales indicate the trend of annual rate (in % per year), where green hues represent a decreasing mangrove disturbance and pink hues represent an increasing mangrove disturbance.

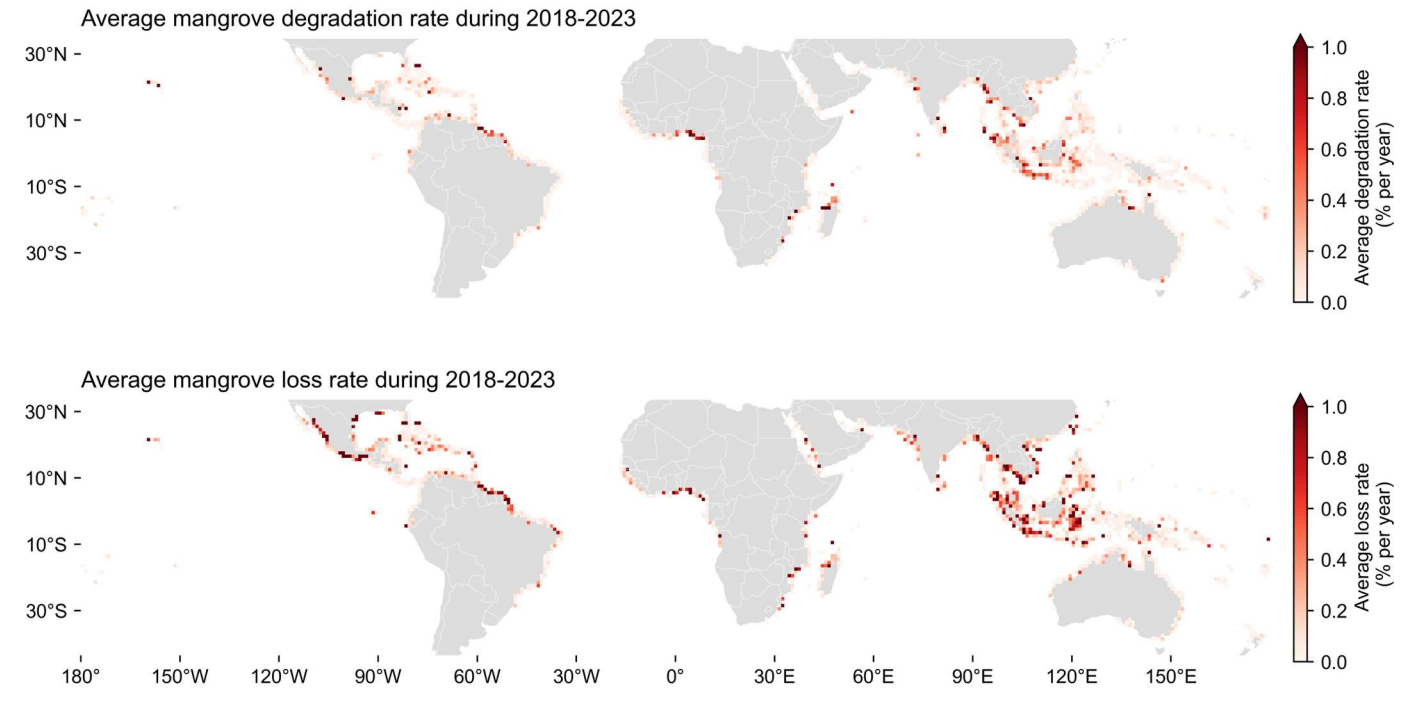


Fig. S9. Global average annual rates of mangrove degradation and loss (2018–2023). Both maps use a common color scale, where darker red hues indicate higher average annual rates (in % per year), and lighter shades/white indicate lower rates, highlighting the spatial distribution of recent mangrove disturbance.

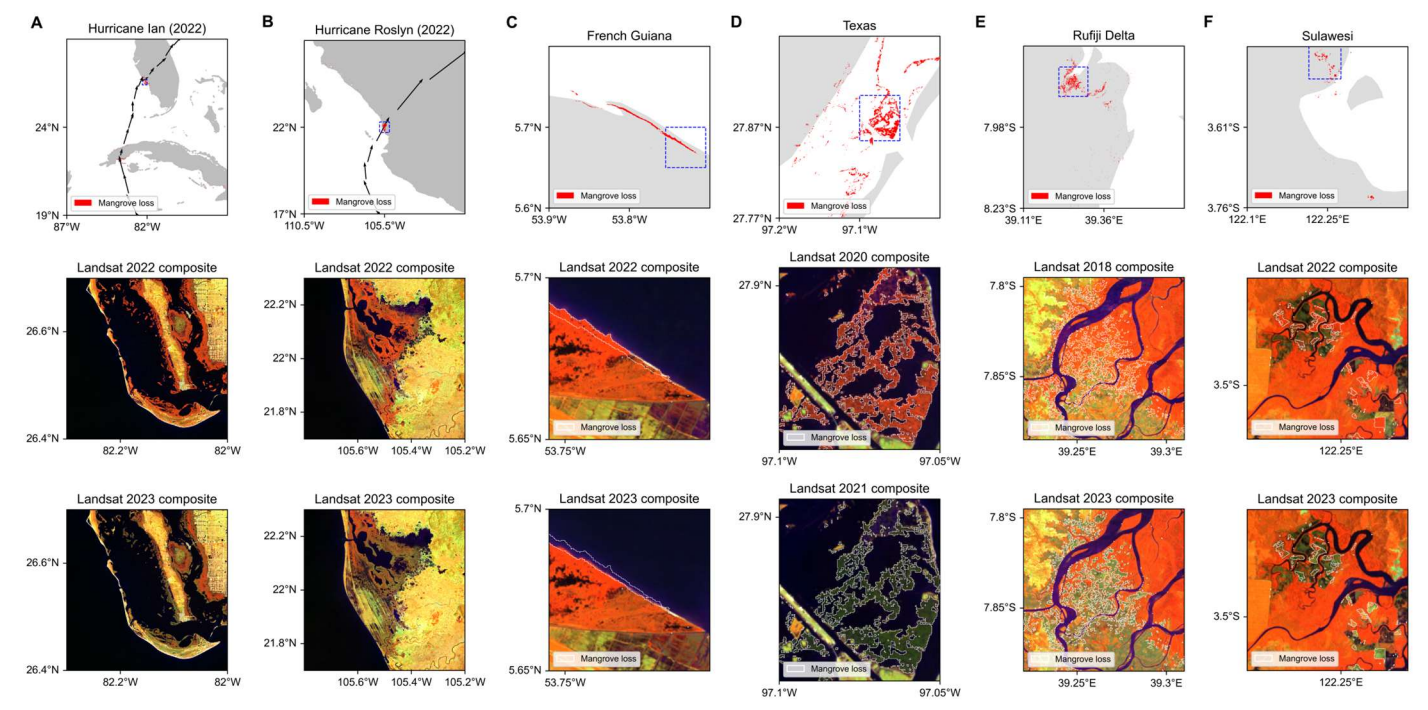


Fig. S10. Local examples of recent mangrove loss events. The top panel provides a contextual map indicating the location and extent of deforestation (red shaded areas). The blue dashed line frame on this map denotes the extent of the Landsat composite imagery shown in the middle (pre-event) and bottom (post-event) panels. White dashed line frames within the Landsat composite images highlight the specific areas of loss. **A** and **B** illustrate mangrove loss caused by tropical cyclones in North America, specifically Hurricane Ian (2022) and Hurricane Roslyn (2022), respectively. **C** shows mangrove loss attributed to shoreline erosion along the Atlantic coast of South America (French Guiana). **D** depicts mangrove loss resulting from an extreme freeze event in Texas, with changes observed between 2020 and 2021. **E** and **F** illustrate ongoing human-driven mangrove deforestation in the Rufiji Delta, Tanzania, and Sulawesi, Indonesia, respectively.

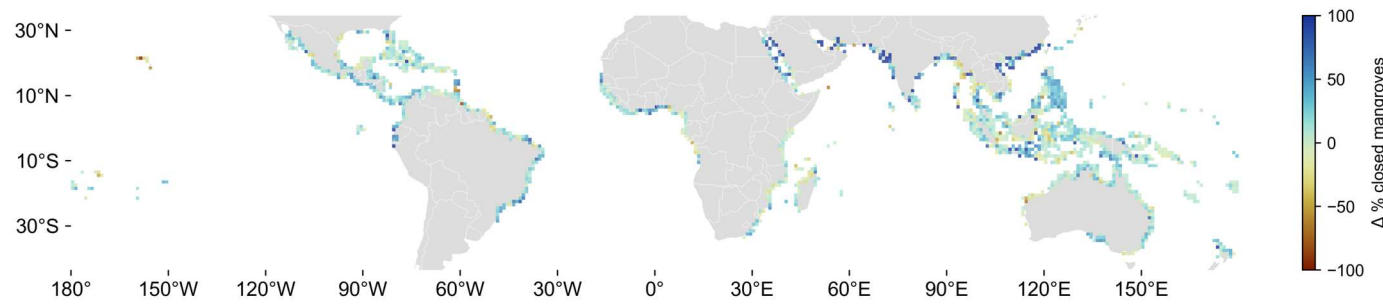


Fig. S11. Global relative change in closed mangrove areas (1980s–2023). This global map illustrates the relative change in closed mangrove areas. The percentage change (Δ % closed mangroves) was calculated as the change in closed mangrove area (Δ closed areas) divided by the total mangrove area in the 1980s. The color scale indicates the percentage change, with blue hues representing increases and brown hues representing decreases. Notably, regions in the Middle East, South Asia, and East Asia exhibit a high relative increase in closed mangrove areas, likely attributed to factors such as range expansion and restoration efforts.

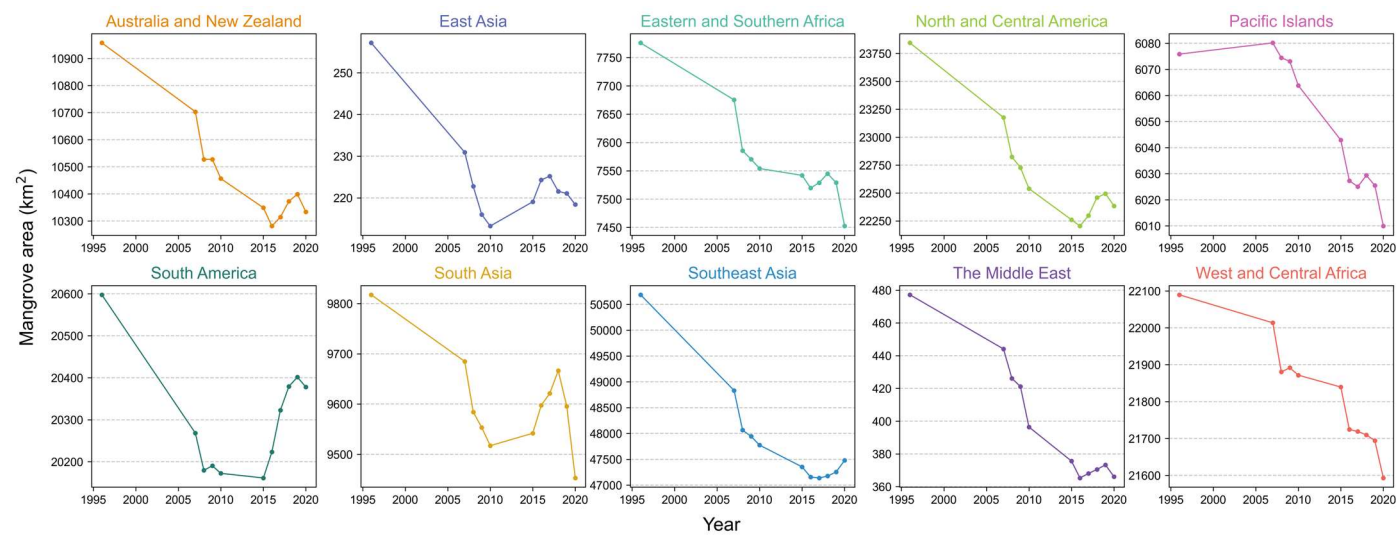


Fig. S12. Mangrove area time series across ten biogeographical regions based on Global Mangrove Watch v3.0. Time series plots illustrate the changes in mangrove area (km²) in each of the ten biogeographical regions from 1996 to 2020. Mangrove area estimates were calculated using the Global Mangrove Watch v3.0 dataset and projected in an equal-area Behrmann coordinate system, consistent with the spatial framework used in our study.

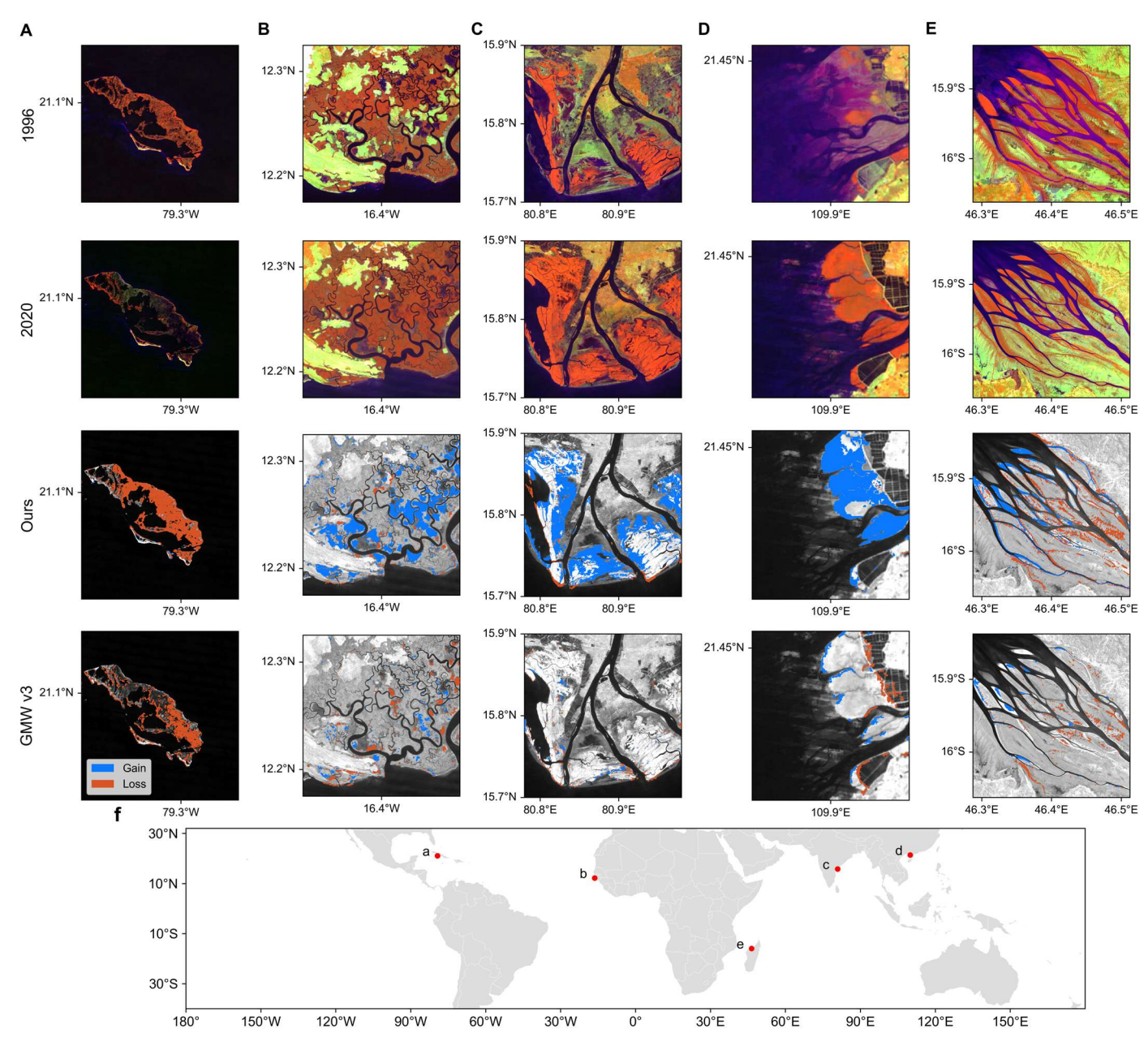
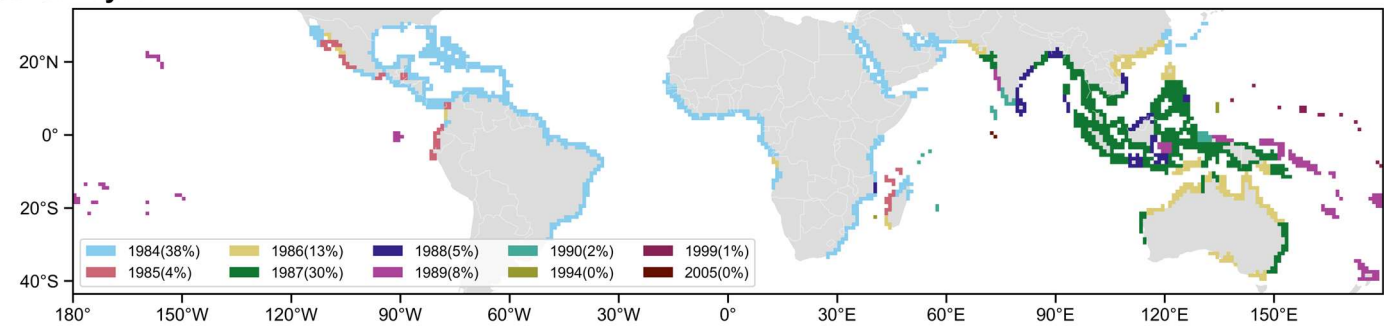
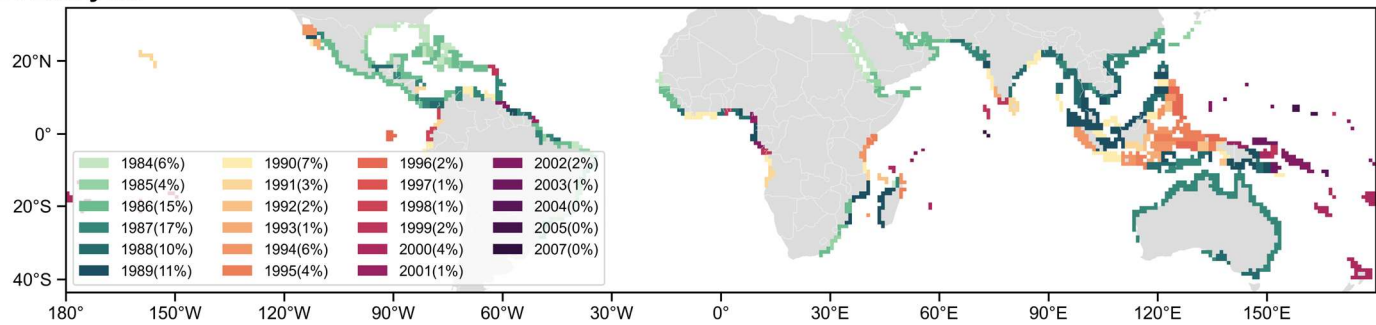


Fig. S13. Comparison of our mangrove change products with Global Mangrove Watch (GMW) v3.0. A detailed comparison was conducted across six representative local sites (A-E). For each site, the first row displays a Landsat composite from 1996, and the second row shows a Landsat composite from 2020. The third row presents our detected mangrove change, overlaid on a 2020 Landsat near-infrared background image, where blue indicates expansion and red indicates deforestation. The fourth row shows the corresponding mangrove change detected by GMW, using the same color scheme. Panel **F** provides a global map indicating the geographic locations of the six comparison sites (A-E). This comparison indicates that GMW underestimates mangrove change globally, particularly mangrove gain (as observed across sites **B-E**).









C. Year span

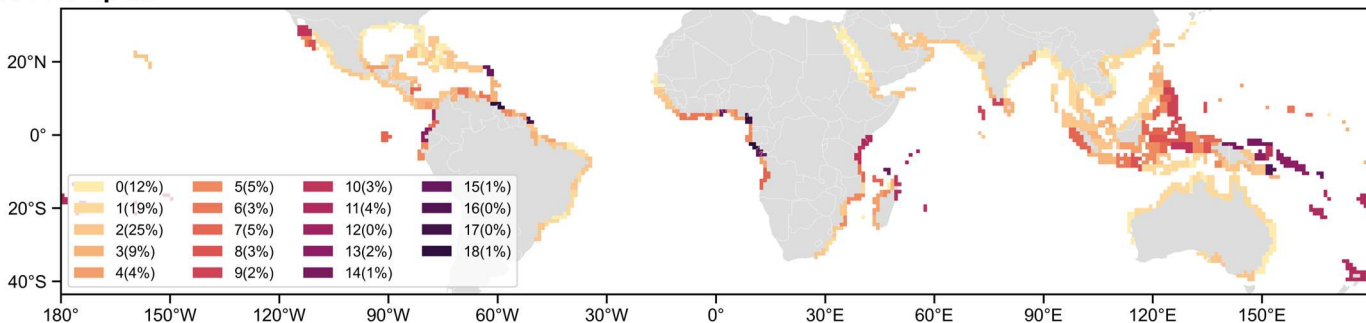
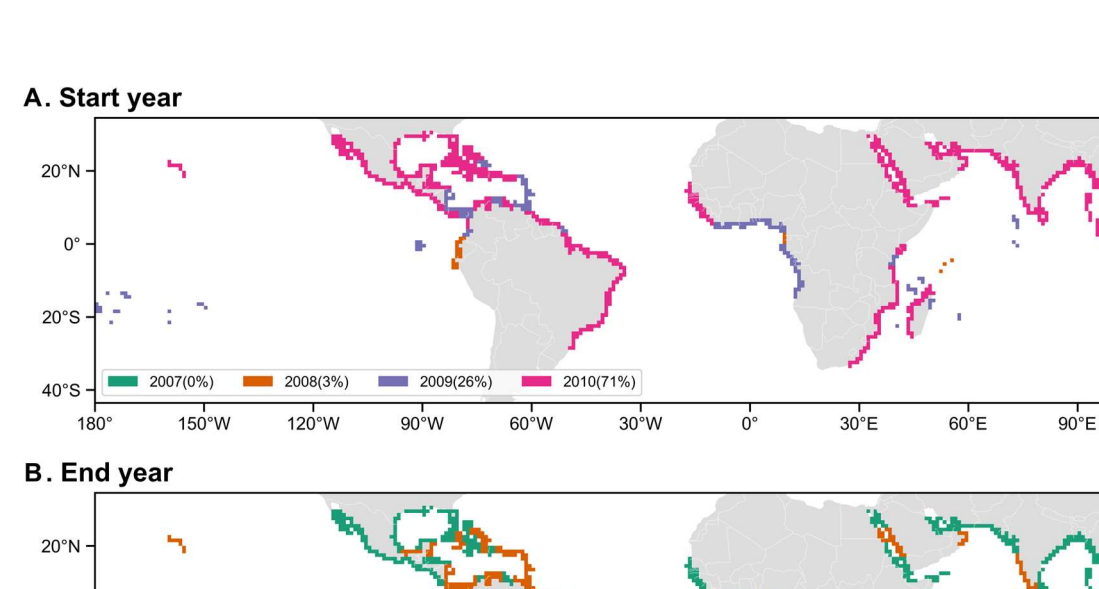
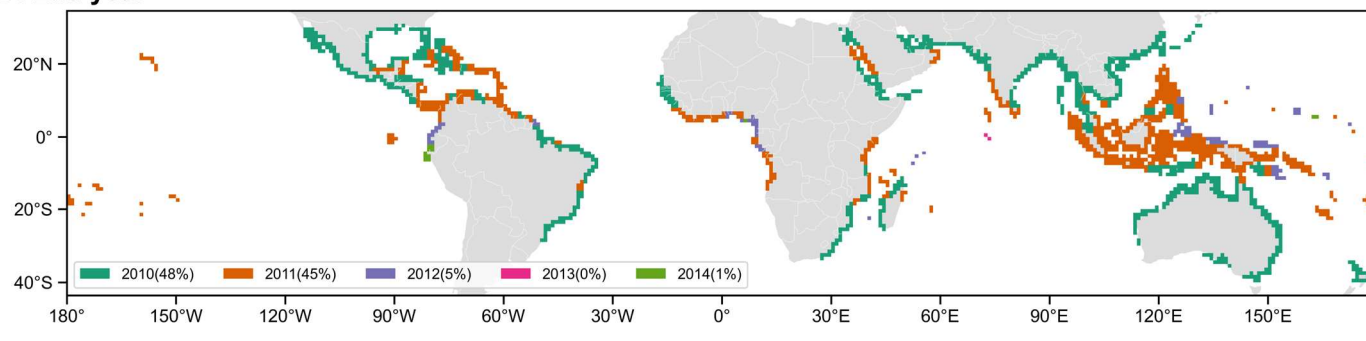


Fig. S14. Temporal composition of the Landsat mosaic used to establish the 1980s mangrove baseline. A, Start year of the annual median Landsat composites used to generate the gap-free mosaic for each grid cell. The legend indicates the different start years and the percentage of the total area represented by each year. B, End year of the annual median Landsat composites used in the mosaic for each grid cell, with corresponding percentages. C, Temporal span (in years) between the start and end year used for compositing each grid cell. For example, a grid cell with a start year of 1984 and an end year of 1986 indicates that annual median composites from 1984, 1985, and 1986 were mosaicked to create a gap-free representation of the 1980s.





120°E

150°E

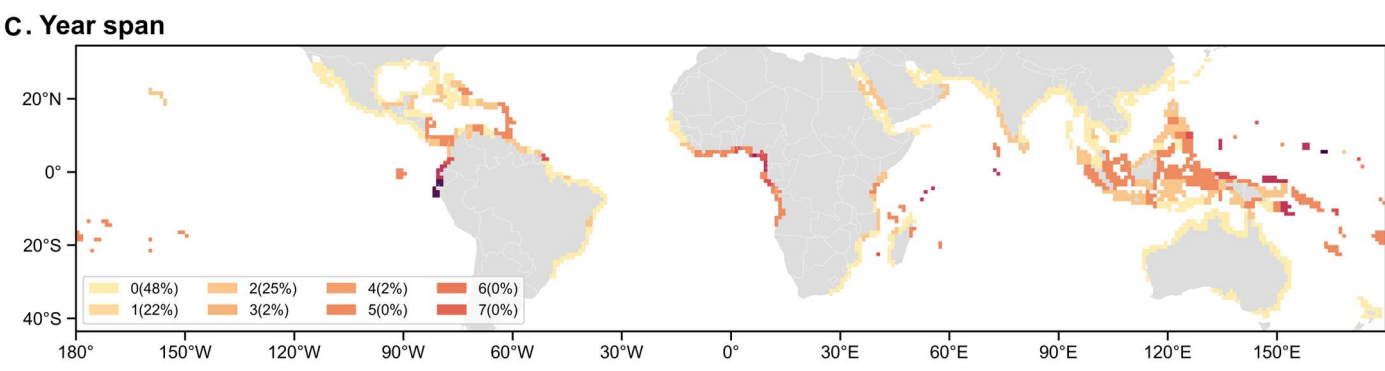


fig. S15. Temporal composition of the Landsat mosaic used to establish the 2010 mangrove baseline. A, Start year of the annual median Landsat composites used to generate the gap-free mosaic for each grid cell. The legend indicates the different start years and the percentage of the total area represented by each year. B, End year of the annual median Landsat composites used in the mosaic for each grid cell, with corresponding percentages. C, Temporal span (in years) between the start and end year used for compositing each grid cell. This indicates the number of annual median composites mosaicked together to create a gap-free representation of the 2010 baseline for each location.

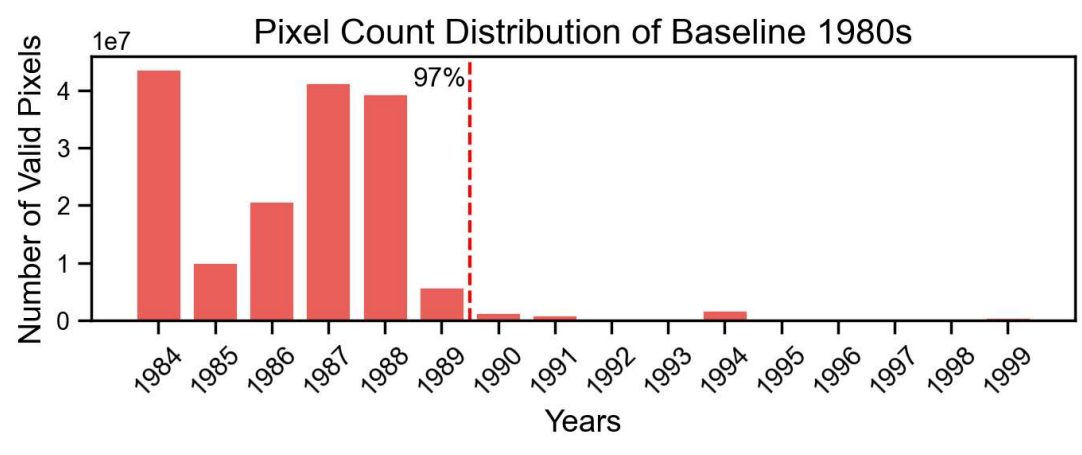


fig. S16. Temporal distribution of Landsat pixels comprising the 1980s mangrove baseline map. Bar plot showing the number of valid 30-meter pixels in the 1980s baseline mangrove map that originated from Landsat imagery acquired in different years. Only years prior to 2000 are shown due to the negligible contribution of later years. The red dashed line indicates that 97% of the baseline map pixels are derived from imagery acquired before 1990.

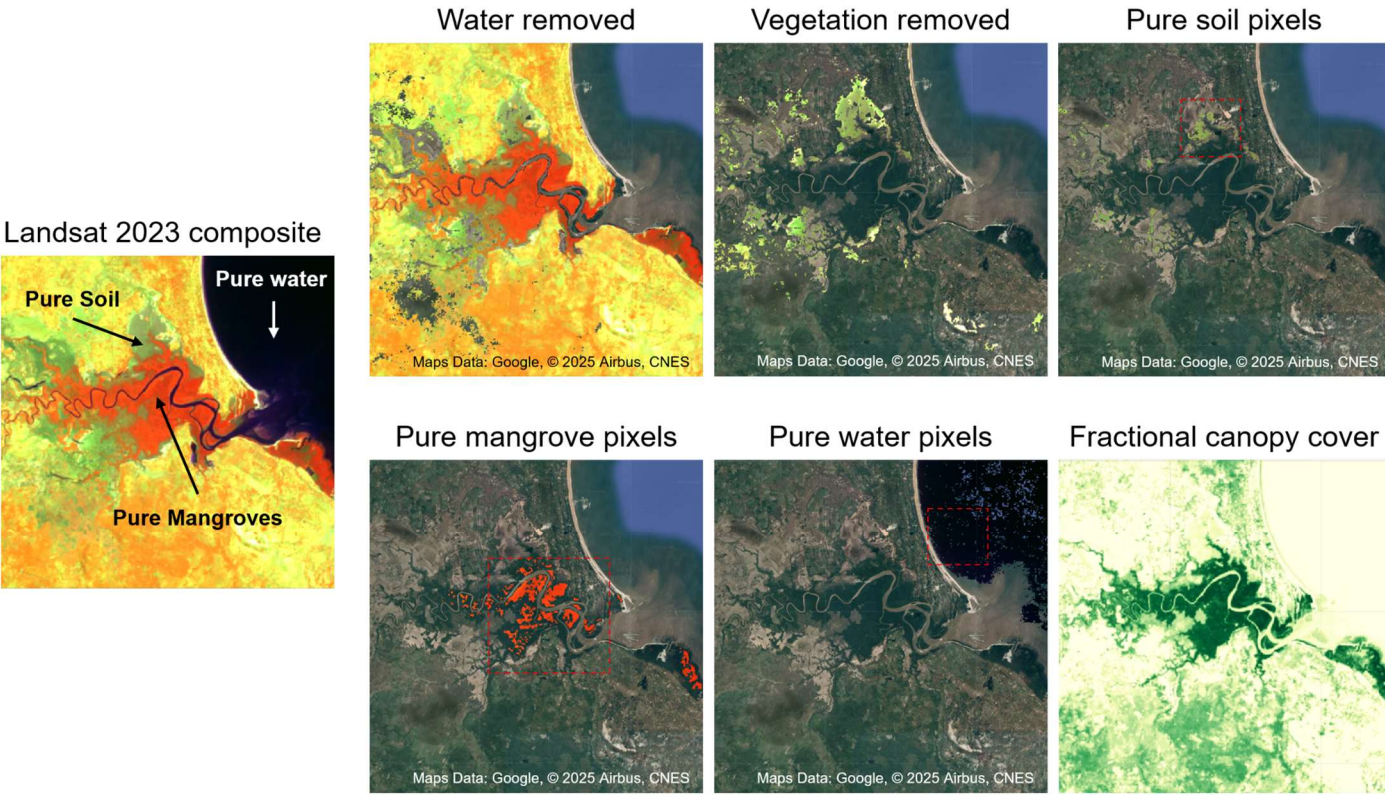


Fig. S17. Process of endmember extraction and Fractional Canopy Cover (FCC) derivation from Landsat imagery. The leftmost panel displays the Landsat 2023 composite with labeled areas representing manually identified pure spectral endmembers (pure soil, pure water, and pure mangroves). The remaining panels show intermediate results of the automatic endmember extraction process. The red dashed boxes highlight iconic endmember areas. The final panel shows the resulting FCC, where greener areas indicate higher FCC (i.e., denser mangrove canopy). High-resolution Google Earth images were shown for reference of the pure pixel types.

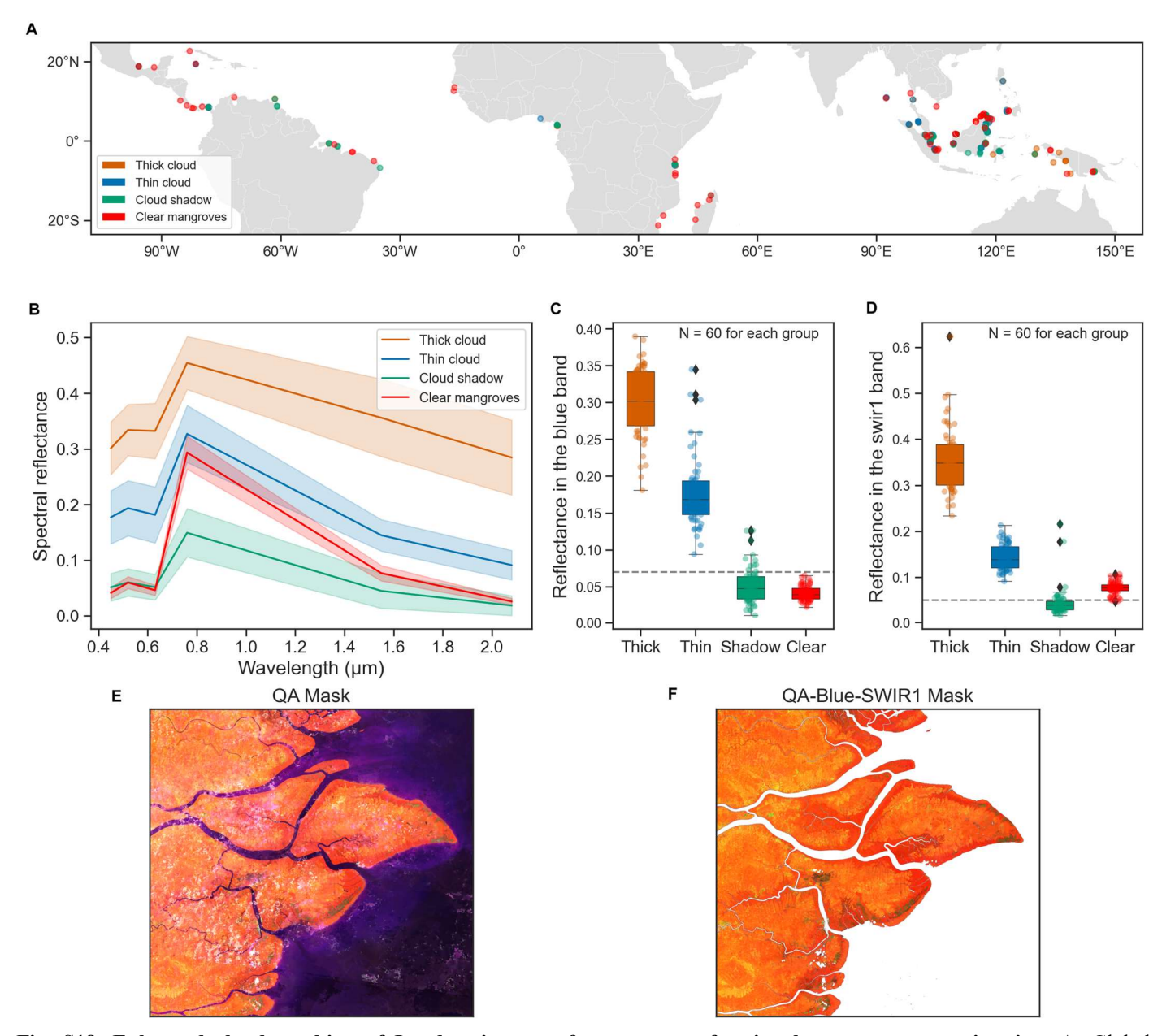


Fig. S18. Enhanced cloud masking of Landsat imagery for mangrove fractional canopy cover estimation. A, Global distribution of the four sample classes used for analysis: thick cloud (orange), thin cloud (blue), cloud shadow (red), and clear mangroves (green). B, Spectral reflectance profiles of the four classes based on Landsat imagery across different wavelengths, with shaded areas indicating 1-fold standard deviation. Box plots showing the reflectance values in the (C) blue band and (D) SWIR1 band for each of the four classes (N = 60 for each group). The dashed line indicates a threshold used for enhanced cloud masking. E, Landsat image of a mangrove area with clouds and shadows, masked using the standard Landsat QA band. F, The same area as in E, showing the improved cloud and shadow masking achieved by incorporating blue and SWIR1 band reflectance characteristics in addition to the QA band.

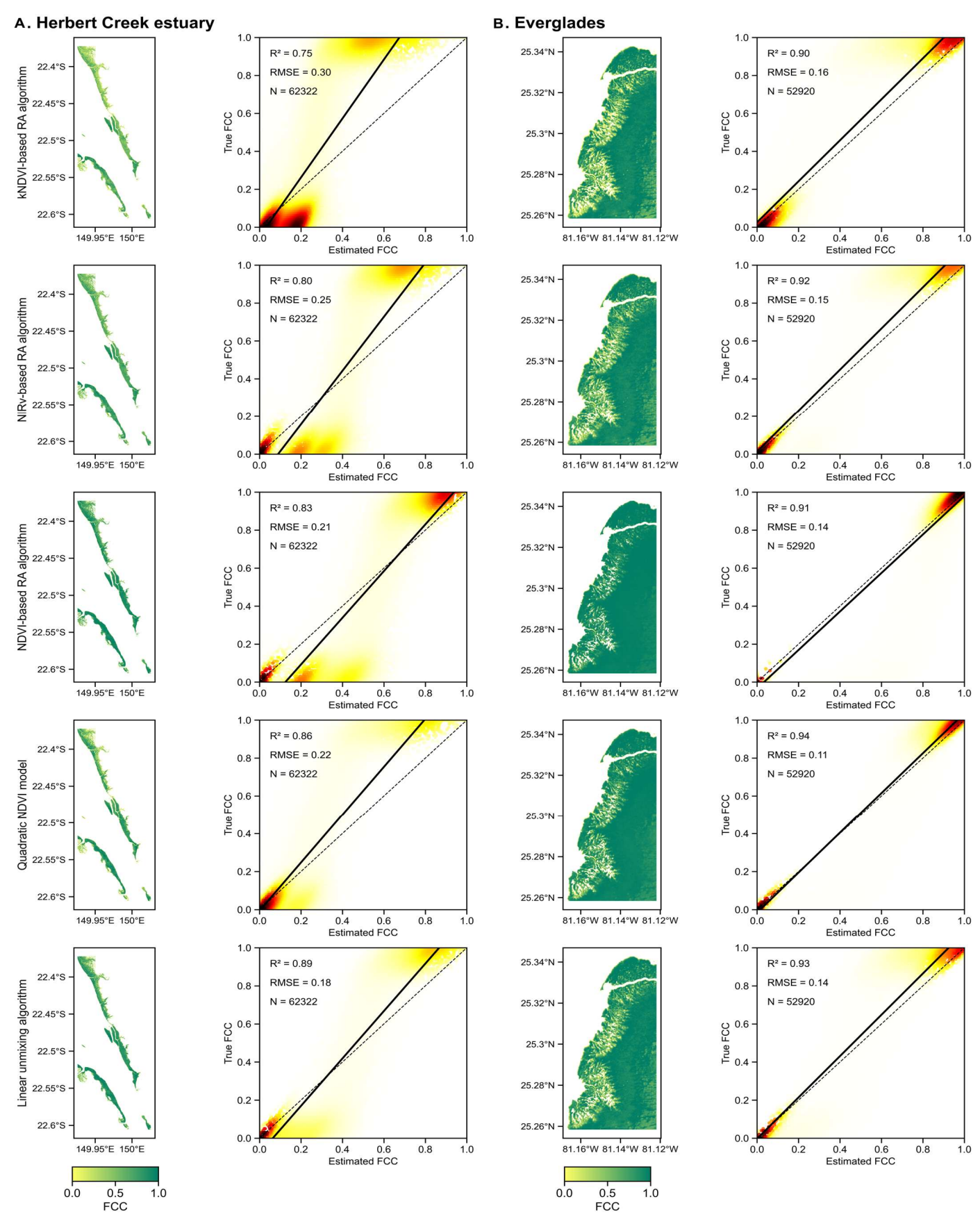


Fig. S19. Validation of five FCC estimation methods at two mangrove sites. Comparison of five different methods for estimating fractional canopy cover (FCC) in **A**, Herbert Creek estuary, and **B**, the Everglades. For each method, the left panel shows the spatial distribution of estimated FCC, and the right panel presents a density scatter plot comparing estimated FCC with true FCC derived from high-resolution PlanetScope SuperDove imagery. The color gradient in the scatter plots indicates the probability density of the data points, with red representing higher densities. The dashed lines represent the 1:1 relationship, and the solid black lines indicate the linear regression fit.

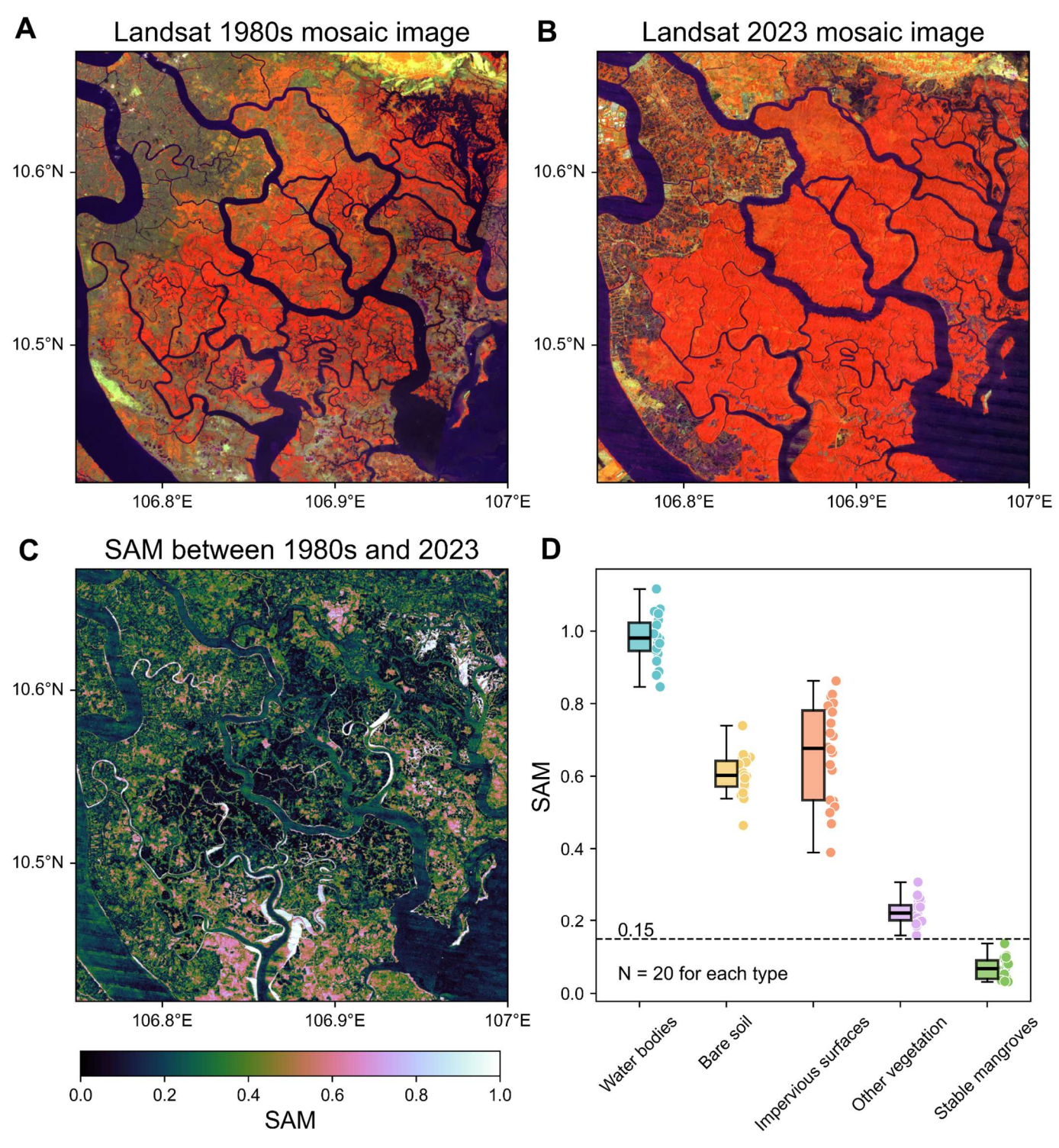


Fig. S20. Spectral Angle Mapper (SAM) for detecting mangrove changes. A, Landsat 1980s mosaic image of the Can Gio Mangrove Biosphere Reserve in Vietnam, composited from 1987 and 1988 data. B, Landsat 2023 mosaic image of the same region. A pronounced gain and growth of mangrove cover (red areas) is evident when compared to the 1980s. C, SAM image calculated from the Landsat 1980s (A) and 2023 (B) mosaics. Larger SAM values represent greater spectral variation between the two time points. D, Distribution of SAM values for five sample types (N = 20 for each type, total N = 100), including water-mangrove transition, bare soil-mangrove transition, impervious surfaces-mangrove transition, other vegetation-mangrove transition, and a stable mangrove category. The central line of boxes represents the median, the box boundaries indicate the 25th and 75th percentiles, and the whiskers extend to 1.5 times the interquartile range; raw data points are overlaid as scatter points. Stable mangroves consistently exhibit very low SAM values, supporting the determination of a 0.15 SAM threshold (dashed line) for identifying mangrove change areas.

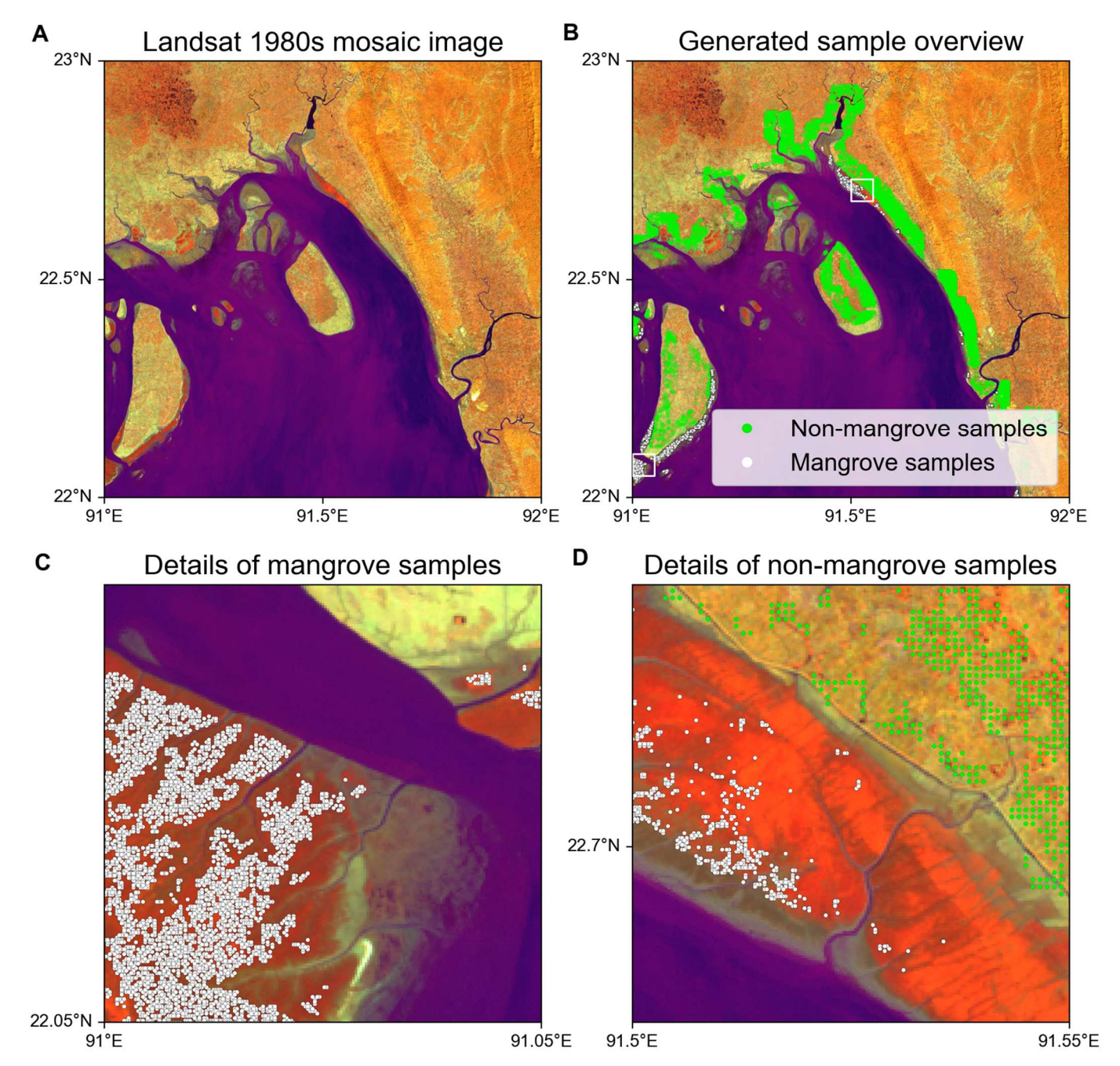


Fig. S21. Evaluation of automatically generated training samples for mangrove mapping. A, Landsat 1980s mosaic image, displayed with near-infrared (NIR), red, and shortwave infrared 1 (SWIR1) bands mapped to red, green, and blue (RGB) channels, respectively, serving as the base imagery. B, Overview of the automatically generated training samples for 1980s. Non-mangrove samples (green dots) and mangrove samples (white dots) overlaid on the mosaic. C, Detailed view of the generated mangrove sample points (white dots) within a mangrove environment (corresponding to the lower white box in B). D, Detailed view of the generated non-mangrove sample points (green dots) within a non-mangrove environment (corresponding to the upper white box in b), showcasing the sampling pattern in non-mangrove areas.

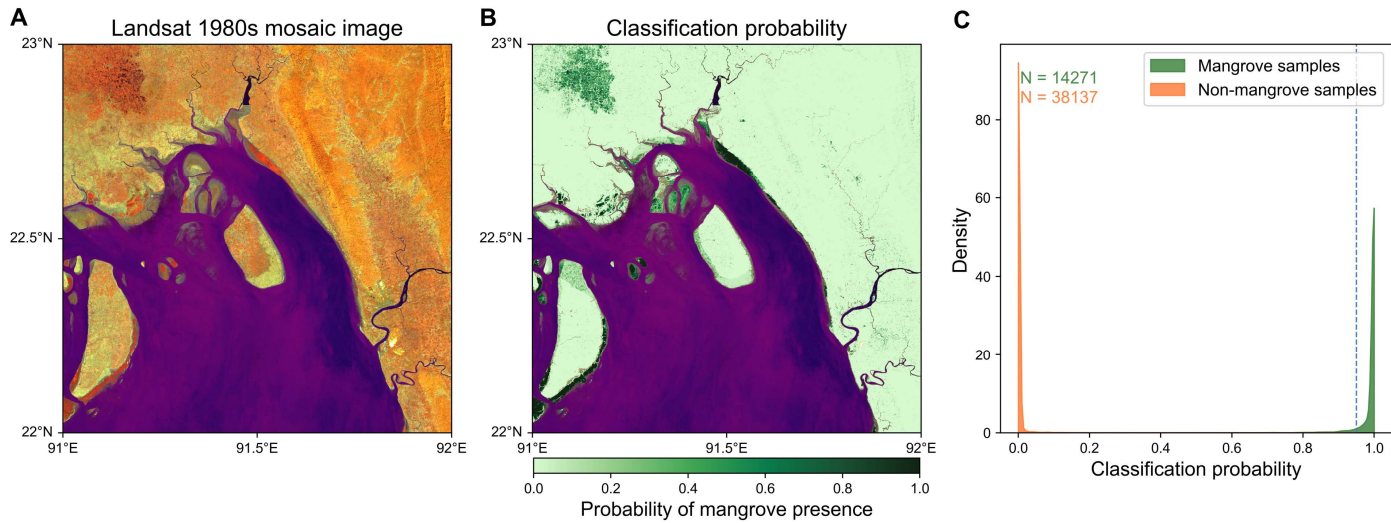


Fig. S22 Classification probability and accuracy assessment of mangrove cover mapping. A, Landsat 1980s mosaic image, serving as the base for classification, displayed with NIR, red, and SWIR1 bands mapped to RGB channels, respectively. B, Spatial distribution of classification probability for mangrove presence. Higher probabilities (indicated by greener hues) represent a greater likelihood of mangrove cover. C, Probability density distribution of classification scores for mangrove and non-mangrove samples. Mangrove samples (green, N = 14,271) predominantly exhibit very high classification probabilities, with over 95% of samples scoring above 0.95 (blue dashed line). Conversely, non-mangrove samples (orange, N = 38,137) consistently show very low classification probabilities, with almost all samples scoring below 0.05, indicating high separability between classes.

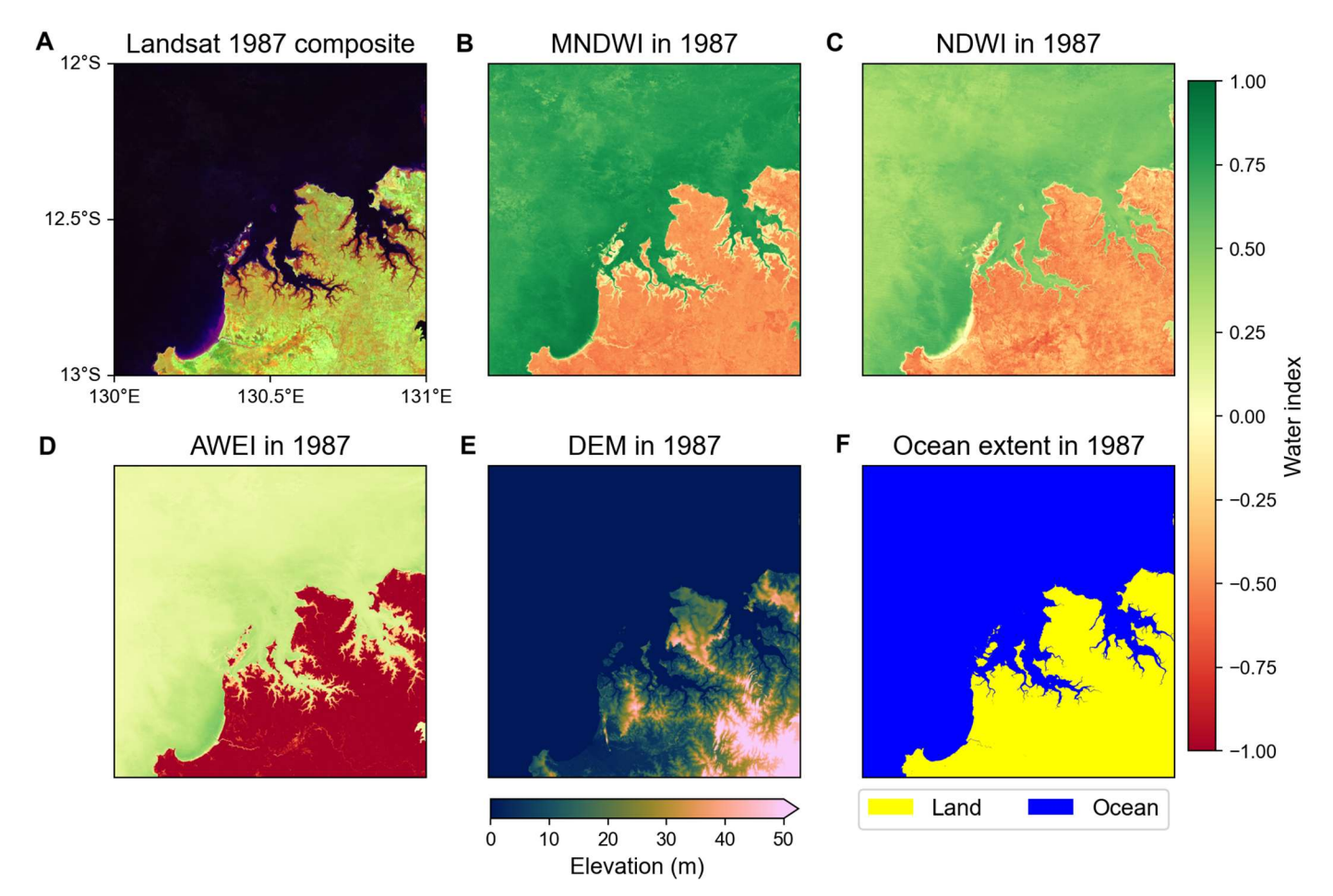


Fig. S23. Example of ocean extent delineation using water indices and digital elevation model. A, Landsat 1987 composite image of the study area. B, Modified Normalized Difference Water Index (MNDWI); C, Normalized Difference Water Index (NDWI); and **D**, Automated Water Extraction Index (AWEI). The common color bar indicates water index values, where greener hues represent higher water probability and warmer hues represent lower water probability. E, Digital Elevation Model (DEM) showing elevation in meters, ranging from 0 m (dark blue) to 50 m (pink). F, Final delineated ocean extent derived from the combined information of the water indices and DEM.

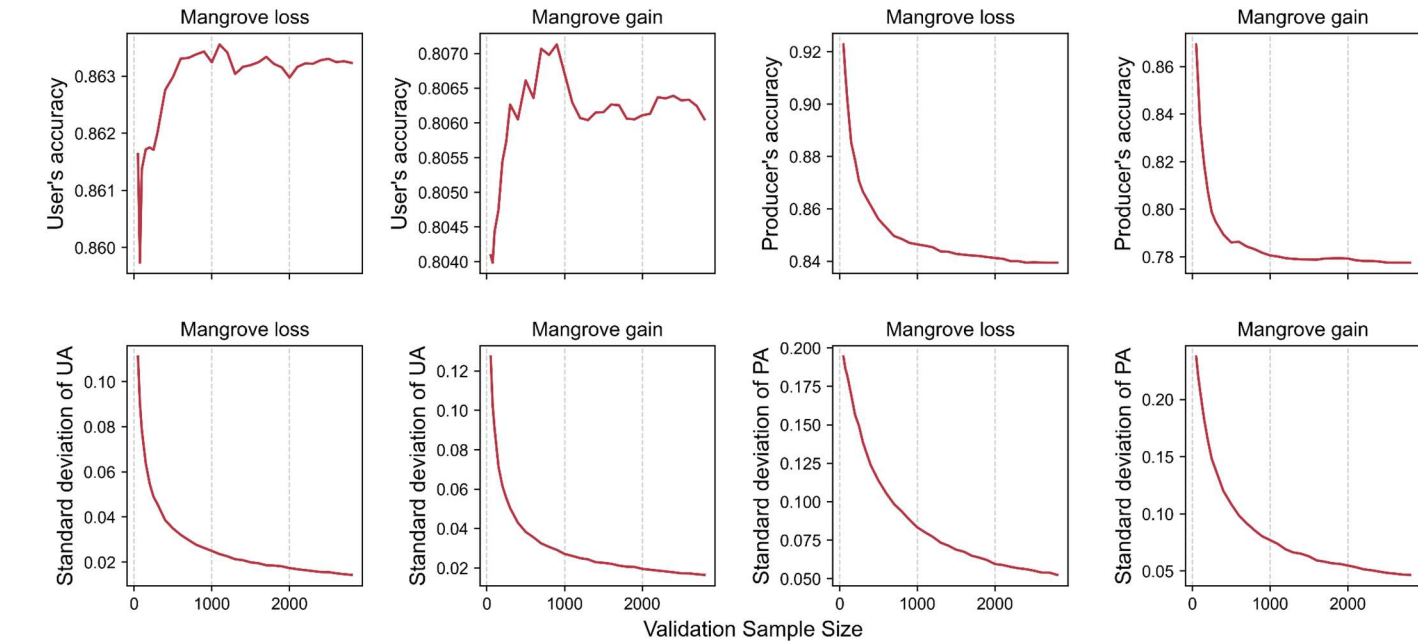


Fig. S24. Sensitivity analysis of accuracy metrics to the number of validation samples. The metrics were derived from a 2000-time bootstrapping process. The upper row shows the mean accuracy (User's Accuracy, UA; and Producer's Accuracy, PA) for both mangrove loss and gain as a function of increasing sample size. UA generally increases with sample size before stabilizing, while PA tends to decrease with sample size before stabilizing. This decrease in PA, which indicates omission error, suggests that larger sample sizes increase the probability of detecting omitted changes. The lower row displays the standard deviation of these accuracy metrics. All standard deviation values consistently decrease as the validation sample size increases, demonstrating that a sample size of approximately 3000 is sufficient to obtain robust and stable accuracy assessments for validating mangrove change detection.

Table S1. Area estimates of mangrove extent and change by biogeographic region from the 1980s to 2023. Areas are in square kilometers. Confidence intervals (CIs) in brackets are from bootstrapping (N = 2000); those reported as \pm are 95% CIs calculated as area \pm 1.96×SE. Sample-based estimation of static mangrove area is not available in our case, because the validation sample set was designed for validating mangrove change types. Net-change CIs for 1980s-2010 and 2010-2023 are computed from paired bootstrap differences, but net-change CIs for 1980s-2023 is computed by differencing net change CIs in 1980s-2010 and 2010-2023 due to lacking an independent validation sample set of 1980s-2023.

]	Mangrove are	ea	Lo	oss	G	ain		Net change	e
	1980s	2010	2023	1980s- 2010	2010- 2023	1980s- 2010	2010- 2023	1980s- 2010	2010- 2023	1980s- 2023
Australia and New Zealand	10009.7	10632.8	10672.8	-278.2	-260.2	901.4	300.1	623.2	39.9	663.1
East Asia	145.4	198.5	301.1	-48.7	-19.4	101.8	122.0	53.1	102.6	155.7
Eastern and Southern Africa	7486.3	7385.4	7385.2	-489.9	-285.7	388.9	285.5	-100.9	-0.2	-101.2
North and Central America	20341.0	20346.6	20562.9	-1410.7	-1157.9	1416.3	1374.2	5.6	216.3	221.9
Pacific Islands	7542.2	7586.3	7578.7	-227.7	-168.3	271.8	160.6	44.1	-7.6	36.5
South Asia	8667.8	9040.6	9575.4	-659.6	-301.7	1032.4	836.5	372.8	534.9	907.7
South America	21373.3	21610.3	21711.3	-1433.3	-909.1	1670.3	1010.1	237.0	101.0	338.0
Southeast Asia	56724.6	52222.5	53253.9	-7498.8	-2507.1	2996.7	3538.5	-4502.1	1031.4	-3470.7
The Middle East	194.5	212.5	341.1	-35.5	-5.5	53.5	134.0	18.0	128.5	146.5
West and Central Africa	22324.9	22692.6	22578.6	-574.4	-659.7	942.1	545.8	367.7	-114.0	253.7
Total	154,809.7	151,928.0	153,960.9	-12,656.9	-6,274.6	9,775.3	8,307.4	-2,881.7	2,032.8	-848.8
Map- based 95% CI		[139,538.5, 154,633.1]						_	[1,131.3, 3,158.4]	[-2,927.4, 1,360.3]
Sample based area (95% CI)	NA	NA	NA	-13,058.9 ±1,577.8	-5,583.1 = 741.7	± 10,161.8 ± 1,195.4	= 7,737.2 ± 678.9	[-4,938.5,	2127.5 [1,131.3, 3,158.4]	-768.5 [-2,927.4, 1,360.3]

Table S2.Accuracy of XGBoost model for annual mangrove degradation area estimation. Mean Absolute Error (MAE) and Mean Absolute Percentage Error (MAPE) were calculated using leave-one-out cross-validation for various regions. MAE is expressed in km², and MAPE is the ratio of MAE to the mean annual mangrove degradation area, presented as a percentage. "Valid observation" indicates the number of years with clear Landsat observations exceeding 60%.

Regions	Mean (km²)	Absolute	Error	Mean Absolute Percentage Error (%)	Valid mangrove observation (ratio ≥ 60%)
Australia and New Zealand	2.11			16.85	35
East Asia	0.19			20.06	36
Eastern and Southern Africa	4.95			26.26	32
North and Central America	11.21			12.74	38
Pacific Islands	1.68			9.64	33
South America	11.66			16.90	36
South Asia	12.27			55.35	34
Southeast Asia	45.55			15.36	34
The Middle East	0.03			14.45	37
West and Central Africa	19.86			16.19	28

Table S3.Accuracy statistics for mangrove extents in baseline years and for 1980s-2010, 1996-2020, and 2010-2023 intervals. Confidence intervals at the 95% level, calculated as 1.96 times standard errors, are shown in parentheses. The error matrices for retrieving these accuracies could be found in table S4-S6.

Map type	Time/Interval	Overall accuracy (%)	User's accuracy (%)	Producer's accuracy (%)
Mangrove extent	1980s	95.1 (0.7)	89.6 (1.6)	93.6 (1.9)
	1996	94.2 (0.8)	90.1 (1.5)	90.0 (2.2)
	2010	95.7 (0.7)	90.6 (1.5)	94.5 (1.8)
	2020	95.8 (0.7)	90.1 (1.5)	95.4 (1.7)
	2023	95.6 (0.8)	93.2 (1.3)	92.0 (2.0)
Mangrove loss	1980s-2010	95.8 (0.7)	86.3 (2.8)	83.7 (9.9)
	1996-2020	96.2 (0.7)	83.6 (3.0)	78.4 (9.3)
	2010-2023	95.5 (0.6)	75.8 (3.4)	85.2 (10.9)
Mangrove gain	1980s-2010	95.8 (0.7)	80.6 (3.2)	77.6 (8.8)
	1996-2020	96.2 (0.7)	78.2 (3.3)	70.8 (12.0)
	2010-2023	95.5 (0.6)	85.0 (2.9)	91.2 (7.5)
Stable mangroves	1980s-2010	95.8 (0.7)	89.0 (2.1)	98.1 (1.2)
	1996-2020	96.2 (0.7)	90.9 (1.9)	97.7 (1.3)
	2010-2023	95.5 (0.6)	95.3 (1.4)	97.5 (1.4)

Table S4.

Error matrices of mangrove change detection between the 1980s and 2010. The matrices summarize sample counts (top) and area-adjusted proportions (bottom) for detected change categories [loss, gain, stable mangroves, and stable non-mangroves (others)] against reference data. Accuracy metrics, including user's accuracy (UA), producer's accuracy (PA), and overall accuracy (OA), are calculated based on area-adjusted proportions.

		Reference							
		Loss	Gain	Stable	Otl	ners	Total		
Detected Change	Loss	517	3	19	60		599		
	Gain	0	483	32	84		599		
	Stable	6	14	799	79		898		
	Others	3	0	4	89	I	898		
	Total	526	500	854	11:	14	2994		
			Refer	rence					
Detected Change	Loss	Loss 0.0210	Gain 0.0001	Stable 0.0008	Others 0.0024	Total 0.0244	UA 86.3%		
change	Gain	0	0.0152	0.0010	0.0026	0.0188	80.6%		
	Stable	0.0018	0.0043	0.2436	0.0241	0.2738	89.0%		
	Others	0.0023	0	0.0030	0.6777	0.6830	99.2%		
	Total	0.0252	0.0196	0.2484	0.7069	1			
	PA	83.7%	77.6%	98.1%	95.9%		OA: 95.8		

Table S5.

Error matrices of mangrove change detection between 2010 and 2023. The matrices summarize sample counts (top) and area-adjusted proportions (bottom) for detected change categories [loss, gain, stable mangroves, and stable non-mangroves (others)] against reference data. Accuracy metrics, including user's accuracy (UA), producer's accuracy (PA), and overall accuracy (OA), are calculated based on area-adjusted proportions.

	Reference								
		Loss	Gai	in	Stable	Others	Total		
Detected Change	Loss	455	3		40	102	600		
	Gain	1	50	8	26	63	598		
	Stable	5	4		856	33	898		
	Others	0	0		7	891	898		
	Total	461	51	5	929	1089	2994		
			Refere	ence					
Detected	Loss	Loss 0.0092	Gain 0.0001	Stable 0.0008	Others 0.0021	Total 0.0121	UA 75.8%		

	Reference									
Detected	Loss	Loss 0.0092	Gain 0.0001	Stable 0.0008	Others 0.0021	Total 0.0121	UA 75.8%			
Change	Gain	0	0.0136	0.0007	0.0017	0.0160	85.0%			
	Stable	0.0016	0.0012	0.2671	0.0103	0.2802	95.3%			
	Others	0	0	0.0054	0.6864	0.6917	99.2%			
	Total	0.0107	0.0149	0.2740	0.7004	1				
	PA	85.2%	91.2%	97.5%	98.0%		OA: 97.6°			

483

PA

78.4%

70.8%

97.7%

96.8%

Table S6.

Error matrices of mangrove change detection between 1996 and 2020. The matrices summarize sample counts (top) and area-adjusted proportions (bottom) for detected change categories [loss, gain, stable mangroves, and stable non-mangroves (others)] against reference data. Accuracy metrics, including user's accuracy (UA), producer's accuracy (PA), and overall accuracy (OA), are calculated based on area-adjusted proportions.

	Reference							
		Loss	Ga	iin	Stable	Others	Total	
Detected Change	Loss	501	501		19	79	599	
	Gain	3	46	59	54	74	600	
	Stable 12		11		816	59	898	
	Others	0	3	3	5	890	898	
	Total	516	48	33	894	1102	2995	
			Refer	rence				
Detected Change	Loss	Loss 0.0137	Gain 0	Stable 0.0005	Others 0.0022	Total 0.0163	UA 83.6%	
S	Gain	0.0001	0.0138	0.0016	0.0022	0.0176	78.2%	
	Stable	0.0037	0.0034	0.2499	0.0181	0.2750	90.9%	
	Others	0	0.0023	0.0038	0.6849	0.6910	99.1%	
	Total	0.0174	0.0195	0.2559	0.7073	1		

OA: 96.2%

REFERENCES AND NOTES

- 1. M. A. Wulder, J. C. White, T. R. Loveland, C. E. Woodcock, A. S. Belward, W. B. Cohen, E. A. Fosnight, J. Shaw, J. G. Masek, D. P. Roy, The global Landsat archive: Status, consolidation, and direction. *Remote Sens. Environ.* **185**, 271–283 (2016).
- 2. N. Gorelick, M. Hancher, M. Dixon, S. Ilyushchenko, D. Thau, R. Moore, Google Earth Engine: Planetary-scale geospatial analysis for everyone. *Remote Sens. Environ.* **202**, 18–27 (2017).
- 3. P. Bunting, A. Rosenqvist, L. Hilarides, R. M. Lucas, N. Thomas, T. Tadono, T. A. Worthington, M. Spalding, N. J. Murray, L.-M. Rebelo, Global Mangrove Extent Change 1996–2020: Global Mangrove Watch Version 3.0. *Remote Sens.* **14**, 3657 (2022).
- 4. M. Jia, Z. Wang, D. Mao, C. Ren, K. Song, C. Zhao, C. Wang, X. Xiao, Y. Wang, Mapping global distribution of mangrove forests at 10-m resolution. *Sci. Bull.* **68**, 1306–1316 (2023).
- 5. C. Giri, E. Ochieng, L. L. Tieszen, Z. Zhu, A. Singh, T. Loveland, J. Masek, N. Duke, Status and distribution of mangrove forests of the world using earth observation satellite data. *Glob. Ecol. Biogeogr.* **20**, 154–159 (2011).
- 6. D. Zanaga, R. Van De Kerchove, W. De Keersmaecker, N. Souverijns, C. Brockmann, R. Quast, J. Wevers, A. Grosu, A. Paccini, S. Vergnaud, O. Cartus, M. Santoro, S. Fritz, I. Georgieva, M. Lesiv, S. Carter, M. Herold, L. Li, N.-E. Tsendbazar, F. Ramoino, O. Arino, ESA WorldCover 10 m 2020 v100, Zenodo (2021); https://zenodo.org/records/5571936.
- 7. X. Zhang, L. Liu, T. Zhao, J. Wang, W. Liu, X. Chen, Global annual wetland dataset at 30 m with a fine classification system from 2000 to 2022. *Sci. Data* 11, 310 (2024).
- 8. J. W. Deardorff, Efficient prediction of ground surface temperature and moisture, with inclusion of a layer of vegetation. *J. Geophys. Res. Oceans* **83**, 1889–1903 (1978).
- 9. S. Wei, H. Zhang, J. Ling, A review of mangrove degradation assessment using remote sensing: advances, challenges, and opportunities. *GIScience Remote Sens.* **62**, 2491920 (2025).
- 10. A. L. Mitchell, A. Rosenqvist, B. Mora, Current remote sensing approaches to monitoring forest degradation in support of countries measurement, reporting and verification (MRV) systems for REDD+. *Carbon Balance Manag.* **12**, 9 (2017).
- 11. M. S. Mon, N. Mizoue, N. Z. Htun, T. Kajisa, S. Yoshida, Factors affecting deforestation and forest degradation in selectively logged production forest: A case study in Myanmar. *For. Ecol. Manag.* **267**, 190–198 (2012).
- 12. J. B. Adams, M. O. Smith, P. E. Johnson, Spectral mixture modeling: A new analysis of rock and soil types at the Viking Lander 1 Site. *J. Geophys. Res. Solid Earth* **91**, 8098–8112 (1986).
- 13. J. de Vries, B. van Maanen, G. Ruessink, P. A. Verweij, S. M. de Jong, Unmixing water and mud: Characterizing diffuse boundaries of subtidal mud banks from individual satellite observations. *Int. J. Appl. Earth Obs. Geoinformation* **95**, 102252 (2021).
- 14. J.-F. Pekel, A. Cottam, N. Gorelick, A. S. Belward, High-resolution mapping of global surface water and its long-term changes. *Nature* **540**, 418–422 (2016).
- 15. S. K. McFeeters, The use of the Normalized Difference Water Index (NDWI) in the delineation of open water features. *Int. J. Remote Sens.* **17**, 1425–1432 (1996).
- 16. C. J. Tucker, Red and photographic infrared linear combinations for monitoring vegetation. *Remote Sens. Environ.* **8**, 127–150 (1979).
- 17. Y. Zha, J. Gao, S. Ni, Use of normalized difference built-up index in automatically mapping urban areas from TM imagery. *Int. J. Remote Sens.* **24**, 583–594 (2003).
- 18. Y. Zhao, Z. Zhu, ASI: An artificial surface Index for Landsat 8 imagery. *Int. J. Appl. Earth Obs. Geoinformation* **107**, 102703 (2022).
- 19. L. Gao, X. Wang, B. A. Johnson, Q. Tian, Y. Wang, J. Verrelst, X. Mu, X. Gu, Remote sensing algorithms for estimation of fractional vegetation cover using pure vegetation index values: A review. *ISPRS J. Photogramm. Remote Sens.* **159**, 364–377 (2020).
- 20. G. Camps-Valls, M. Campos-Taberner, Á. Moreno-Martínez, S. Walther, G. Duveiller, A. Cescatti, M. D. Mahecha, J. Muñoz-Marí, F. J. García-Haro, L. Guanter, M. Jung, J. A. Gamon, M. Reichstein, S. W. Running, A unified vegetation index for quantifying the terrestrial biosphere. *Sci. Adv.* 7, eabc7447 (2021).
- 21. G. Badgley, C. B. Field, J. A. Berry, Canopy near-infrared reflectance and terrestrial photosynthesis. *Sci. Adv.* **3**, e1602244 (2017).
- 22. A. B. Baloloy, A. C. Blanco, R. R. C. Sta. Ana, K. Nadaoka, Development and application of a new mangrove vegetation index (MVI) for rapid and accurate mangrove mapping. *ISPRS J. Photogramm. Remote Sens.* **166**, 95–117 (2020).
- 23. C. Diniz, L. Cortinhas, G. Nerino, J. Rodrigues, L. Sadeck, M. Adami, P. W. M. Souza-Filho, Brazilian Mangrove Status: Three Decades of Satellite Data Analysis. *Remote Sens.* **11**, 808 (2019).
- 24. F. A. Kruse, A. B. Lefkoff, J. W. Boardman, K. B. Heidebrecht, A. T. Shapiro, P. J. Barloon, A. F. H. Goetz, The spectral image processing system (SIPS)—interactive visualization and analysis of imaging spectrometer data. *Remote Sens. Environ.* 44, 145–163 (1993).

- 25. H. Xu, Modification of normalised difference water index (NDWI) to enhance open water features in remotely sensed imagery. *Int. J. Remote Sens.*, doi: 10.1080/01431160600589179 (2006).
- 26. T. Hermosilla, M. A. Wulder, J. C. White, N. C. Coops, Land cover classification in an era of big and open data: Optimizing localized implementation and training data selection to improve mapping outcomes. *Remote Sens. Environ.* **268**, 112780 (2022).
- 27. L. Breiman, Random Forests. *Mach. Learn.* **45**, 5–32 (2001).

- 28. Z. Zhang, N. Xu, Y. Li, Y. Li, Sub-continental-scale mapping of tidal wetland composition for East Asia: A novel algorithm integrating satellite tide-level and phenological features. *Remote Sens. Environ.* **269**, 112799 (2022).
- 29. N. J. Murray, S. R. Phinn, M. DeWitt, R. Ferrari, R. Johnston, M. B. Lyons, N. Clinton, D. Thau, R. A. Fuller, The global distribution and trajectory of tidal flats. *Nature* **565**, 222–225 (2019).
- 30. S. M. Hickey, B. Radford, Turning the Tide on Mapping Marginal Mangroves with Multi-Dimensional Space—Time Remote Sensing. *Remote Sens.* **14**, 3365 (2022).
- 31. M. C. Hansen, P. V. Potapov, R. Moore, M. Hancher, S. A. Turubanova, A. Tyukavina, D. Thau, S. V. Stehman, S. J. Goetz, T. R. Loveland, A. Kommareddy, A. Egorov, L. Chini, C. O. Justice, J. R. G. Townshend, High-resolution global maps of 21st-century forest cover change. *Science* **342**, 850–853 (2013).
- 32. G. L. Feyisa, H. Meilby, R. Fensholt, S. R. Proud, Automated Water Extraction Index: A new technique for surface water mapping using Landsat imagery. *Remote Sens. Environ.* **140**, 23–35 (2014).
- 33. Z. Zhu, Change detection using landsat time series: A review of frequencies, preprocessing, algorithms, and applications. *ISPRS J. Photogramm. Remote Sens.* **130**, 370–384 (2017).
- 34. N. J. Murray, T. A. Worthington, P. Bunting, S. Duce, V. Hagger, C. E. Lovelock, R. Lucas, M. I. Saunders, M. Sheaves, M. Spalding, N. J. Waltham, M. B. Lyons, High-resolution mapping of losses and gains of Earth's tidal wetlands. *Science* **376**, 744–749 (2022).
- 35. Q. Zhang, Z. Zhang, N. Xu, Y. Li, Fully automatic training sample collection for detecting multi-decadal inland/seaward urban sprawl. *Remote Sens. Environ.* **298**, 113801 (2023).
- 36. Z. Zhang, M. R. Ahmed, Q. Zhang, Y. Li, Y. Li, Monitoring of 35-Year Mangrove Wetland Change Dynamics and Agents in the Sundarbans Using Temporal Consistency Checking. *Remote Sens.* **15**, 625 (2023).
- 37. C. Vancutsem, F. Achard, J.-F. Pekel, G. Vieilledent, S. Carboni, D. Simonetti, J. Gallego, L. E. O. C. Aragão, R. Nasi, Long-term (1990–2019) monitoring of forest cover changes in the humid tropics. *Sci. Adv.* 7, eabe1603 (2021).
- 38. L. Lymburner, P. Bunting, R. Lucas, P. Scarth, I. Alam, C. Phillips, C. Ticehurst, A. Held, Mapping the multi-decadal mangrove dynamics of the Australian coastline. *Remote Sens. Environ.* **238**, 111185 (2020).
- 39. T. Chen, C. Guestrin, "XGBoost: A Scalable Tree Boosting System" in *Proceedings of the 22nd ACM SIGKDD International Conference on Knowledge Discovery and Data Mining* (Association for Computing Machinery, New York, NY, USA, 2016; https://dl.acm.org/doi/10.1145/2939672.2939785)*KDD '16*, pp. 785–794.
- 40. P. Olofsson, G. M. Foody, M. Herold, S. V. Stehman, C. E. Woodcock, M. A. Wulder, Good practices for estimating area and assessing accuracy of land change. *Remote Sens. Environ.* **148**, 42–57 (2014).